## Reduced-gradient analysis of van der Waals complexes

T. Jenkins, <sup>1, 2</sup> K. Berland, <sup>3, \*</sup> and T. Thonhauser <sup>1, 2, †</sup>

<sup>1</sup>Department of Physics, Wake Forest University, Winston-Salem, NC 27109, USA.
<sup>2</sup>Center for Functional Materials, Wake Forest University, Winston-Salem, NC 27109, USA.
<sup>3</sup>Faculty of Science and Technology, Norwegian University of Life Sciences, Norway.

(Dated: October 13, 2021)

Different methods to describe dispersion interactions within density functional theory have been developed, which is essential to describe binding in van der Waals complexes. However, several key aspects of such complexes—including binding energies, lattice constants, and binding distancesalso depend on the exchange description that is paired with the description of dispersion interactions. This is particularly true for the vdW-DF family of van der Waals density functionals, which has a clear division between truly non-local correlations and semi-local generalized-gradient exchange. Here, we present a systematic analysis of the reduced-gradient values that determine the semilocal exchange for different classes of van der Waals complexes. In particular, we analyze molecular dimers, layered structures, surface adsorption, and molecular crystals. We find that reduced-gradient values of less than  $\sim 1$  to  $\sim 1.5$ —depending on the system—contribute attractively to the exchange binding, while reduced gradients above those values are repulsive. We find that the attractive contributions can be attributed to low-density regions between the constituents with disk-like isosurfaces. We further identify a mechanism wherein the surface area of these disks decreases through merging with other iso-surfaces and switches the gradient-correction to exchange from attractive to repulsive. This analysis allows us to explain some of the differences in performance of vdW-DF variants and initiates a discussion of desirable features of the exchange enhancement factor. While our analysis is focused on vdW-DF, it also casts light on van der Waals binding in a broader context and can be used to understand why methods perform differently for different classes of van der Waals systems.

#### I. INTRODUCTION

van der Waals interactions provide crucial contributions to the binding and structure of an evergrowing list of technologically relevant materials, reaching from photovoltaics and organic electronics, 1-4 to ferroelectrics,  $^{5,6}$  pharmaceuticals,  $^7$  and applications in gas storage/sequestration,  $^{8-10}$  sensing,  $^{11}$  and catalysis.  $^{12}$ Density functional theory has long struggled to correctly describe those materials, but over the last two decades numerous approaches have been developed to overcome this problem. <sup>13–30</sup> Among these, the vdW-DF family <sup>27–32</sup> of non-local density functionals is of particular interest because it can describe van der Waals interactions based on knowledge of the electron density  $n(\mathbf{r})$  alone. The latest release of this family, i.e. vdW-DF3,<sup>32</sup> exhibits the highest accuracy for different classes of dispersionbonded systems in the vdW-DF family. However, during the construction of vdW-DF3 it became apparent that further efforts to improve its accuracy are inhibited by a lack of in-depth understanding of the mechanisms causing different vdW-DF variants to perform differently for different classes of systems.

The van der Waals interactions within vdW-DF are captured through a non-local correlation contribution to the exchange-correlation energy.<sup>27,30</sup> This non-local correlation functional provides the majority of the en-

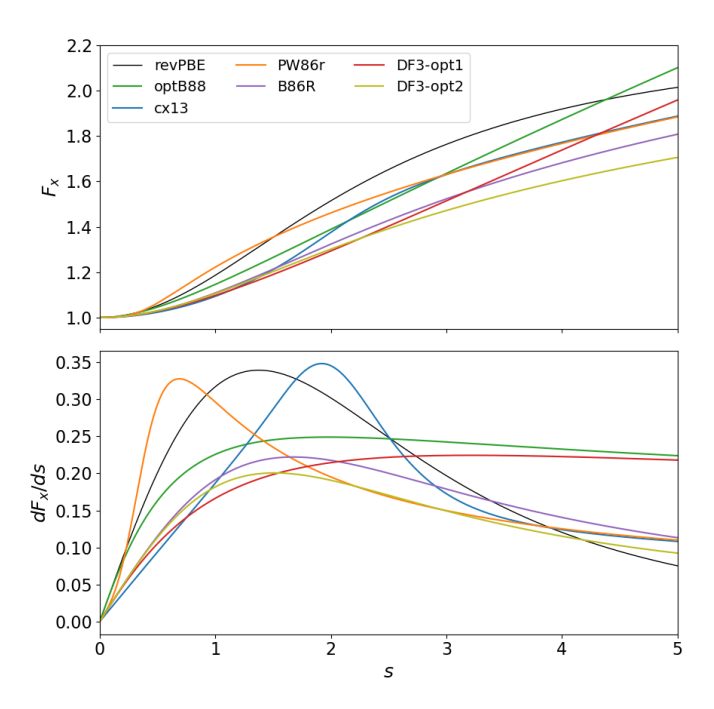


FIG. 1. (top) Exchange enhancement factors  $F_x(s)$  used in various vdW-DF variants and (bottom) their derivatives.

ergetics that contributes to the binding of van der Waals complexes. However, the remainder of the exchange-correlation functional—in particular the semilocal exchange—plays a crucial role in determining structural aspects such as binding separations or lattice constants. Within the generalized-gradient approximation

<sup>\*</sup> E-mail: kristian.berland@nmbu.no

<sup>†</sup> E-mail: thonhauser@wfu.edu

(GGA),<sup>33</sup> the semi-local exchange is typically expressed in terms of an exchange enhancement factor  $F_{\mathbf{x}}(s)$ , which describes gradient corrections to the local density approximation (LDA) in terms of the reduced gradient  $s(\mathbf{r}) \propto |\nabla n(\mathbf{r})|/n(\mathbf{r})^{4/3}$ . Various exchange enhancement factors used in the vdW-DF family are plotted in Fig. 1 and lead to quite different results for different classes of van der Waals complexes. 32 Different features of  $F_{x}(s)$ and its derivative play an important role in determining the various aspects of van der Waals systems, possibly leading to competing requirements for  $F_{\rm x}(s)$  to achieve high accuracy, as discussed for molecular dimers vs. molecular crystals in Ref. [32]. In this paper, we provide a systematic analysis of which values of s are most important for different systems. This allows us to explain some of the performance differences of the various exchanges that have been used throughout the history of the vdW-DF development, and it also forms the basis for identifying desirable features of the exchange enhancement factor. Such an s-analysis has a long history for general systems<sup>34–36</sup> and was first applied to a limited set of van der Waals complexes in Ref. [37]. While our paper emphasizes a quantitative analysis of energetic and force contributions to vdW-DF, our analysis can also provide a starting point to understand and improve other schemes to include dispersion interactions in density functional theory. In addition, our reduced-gradient analysis can also be used to assess the nature and existence of noncovalent bonding from a method-independent perspective following Refs. [38, 39].

## II. THEORY

Within the vdW-DF framework, the exchange-correlation energy  $E_{\rm xc}$  is given by

$$E_{\rm xc}[n] = E_{\rm x}^{\rm GGA}[n] + E_{\rm c}^{\rm LDA}[n] + E_{\rm c}^{\rm nl}[n] \; . \eqno(1)$$

Here, the semi-local exchange  $E_{\rm x}^{\rm GGA}[n]$  is given at the GGA level, the purely local correlation  $E_{\rm c}^{\rm LDA}[n]$  is evaluated at the LDA level, and the non-local contribution is given by

$$E_{\rm c}^{\rm nl}[n] = \frac{1}{2} \int d^3 \mathbf{r} \int d^3 \mathbf{r}' \ n(\mathbf{r}) \, \Phi(\mathbf{r}, \mathbf{r}') \, n(\mathbf{r}') \ , \qquad (2)$$

where the kernel  $\Phi(\mathbf{r}, \mathbf{r}')$  is a function of the charge density and its gradient at the points  $\mathbf{r}$  and  $\mathbf{r}'$ . Note the lack of gradient corrections to the local correlation in Eq. (1),<sup>30</sup> which ensures that there is no double-counting of semi-local correlation contributions. The non-local contribution is derived from a many-body starting point and observes four physical constraints. <sup>30,40–43</sup> The semi-local exchange is typically expressed as

$$E_{\mathbf{x}}^{\mathrm{GGA}}[n] = \int d^{3}\mathbf{r} \ n(\mathbf{r}) \, \epsilon_{\mathbf{x}}^{\mathrm{hom}}(n(\mathbf{r})) \, F_{\mathbf{x}}(s) \ , \tag{3}$$

and describes the enhancement (through the exchange enhancement factor  $F_{\rm x}(s)$ ) over the exchange of the homogeneous electron gas  $\epsilon_{\rm x}^{\rm hom}$ . It is Eq. (2) that allows vdW-DF to capture van der Waals interactions<sup>30</sup> and distinguishes the vdW-DF family from other, popular semilocal functionals such as PBE<sup>33</sup> and hybrid functionals such as PBE0<sup>44</sup> and B3LYP<sup>45</sup> (which do not have an explicit mechanism to describe long-range London dispersion forces and are thus often paired with C<sub>6</sub>-based correction schemes such as DFT-D3<sup>46</sup>). Note that hybrid functionals include a fraction of the exact exchange in conjunction with a density functional like Eq. (3).

Much research has gone into improving the exchange enhancement factor within vdW-DF. The original choice of revPBE<sup>47,48</sup> for the GGA-type exchange in vdW-DF1, with its rapidly increasing  $F_{\rm x}(s)$  in the s=0.5-2 range (see Fig. 1), avoids nonphysical exchange-based binding in van der Waals systems at binding separations.<sup>27,37</sup> However, that same choice of revPBE is also responsible for the too large binding separations observed with vdW-DF1.<sup>49-52</sup> Further research indicated that  $F_{\rm x}(s) \propto s^{2/5}$  in the limit of large s also avoids such non-physical binding using a formal argument and can provide good agreement with Hartree-Fock calculations.<sup>37</sup> This argument was used to support the use of PW86r in vdW-DF2.<sup>53</sup> It has also been shown that the separation overestimation in vdW-DF1 can be avoided by using an  $F_{\mathbf{x}}(s)$  that increases more slowly with s for small values of s < 1.54

Clearly, the features of  $F_{\rm x}(s)$ , in particular for values 0 < s < 3, have a profound impact on van der Waals complexes. But, in order to make improvements, we have to identify which s values in that range are the most important for a particular class of complexes and deduce desirable shapes of  $F_{\rm x}(s)$  in more limited ranges of s to improve a particular class of systems. To identify s values important for the binding of van der Waals complexes, we compute the s-resolved exchange interaction energy as the difference between the GGA and LDA values s-resolved.

$$\Delta e_{\rm gx}(s) = e_{\rm gx}^{\rm tot}(s) - \sum_{i} e_{\rm gx}^{i}(s) , \qquad (4)$$

where the "tot" superscript refer to the total system and "i" refers to the individual fragments. The individual gradient portions of the exchange energy are calculated as

$$e_{\rm gx}(s) = -\frac{3}{4} \left(\frac{3}{\pi}\right)^{1/3} \int d^3 \mathbf{r} \ n^{4/3} \left[ F_{\rm x} \left( s(\mathbf{r}) \right) - 1 \right] \delta \left( s - s(\mathbf{r}) \right) , \tag{5}$$

where the  $[F_{\mathbf{x}}(s(\mathbf{r})) - 1]$  singles-out the purely semilocal gradient corrections to exchange by removing contributions from the local LDA exchange, which all vdW-DF functional have in common.<sup>55</sup> Similarly, in Eq. (1) all vdW-DF functionals have the same local correlation  $E_{\mathbf{c}}^{\mathrm{LDA}}$ , allowing us to relate performance differences mostly to differences in semi-local gradient exchange, Eq. (5), for all functionals that share the same  $E_{\mathbf{c}}^{\mathrm{nl}}$ . The main focus of our analysis will be the comparison of  $\Delta e_{\rm gx}(s)$  from Eq. (4) for various different classes of van der Waals complexes as well as different functionals of the vdW-DF family. Another property of interest is the s-integrated quantity

$$\Delta E_{\rm gx}(s) = \int_0^s ds' \, \Delta e_{\rm gx}(s') \,. \tag{6}$$

Then,  $\Delta E_{\rm gx}(\infty)$  gives the total gradient-corrected exchange portion of the interaction energy.

For an analysis of binding separations, the corresponding forces are essential. In parallel to the s-resolved exchange energy  $\Delta e_{\rm gx}(s)$  we define a s-resolved exchange force  $\Delta k_{\rm gx}(s)$  as the energy derivative

$$\Delta k_{\rm gx}(s) = -\frac{\mathrm{d}\Delta e_{\rm gx}(s)}{\mathrm{d}|a|}, \qquad (7)$$

where **a** is a suitably defined separation between fragments of the van der Waals complex. Such forces are related to the exchange *potential*, which in turn includes terms of the form  $dF_{\rm x}(s)/ds.^{56,57}$  Performance with respect to binding separations will thus make connections to the bottom panel of Fig. 1. Similarly to Eq. (6), we define the s-integrated quantity  $\Delta K_{\rm gx}(s)$ ; where  $\Delta k_{\rm gx}(s)$  is analogous to  $\Delta e_{\rm gx}(s)$ ,  $\Delta K_{\rm gx}(s)$  is the integrated analogue to  $\Delta E_{\rm gx}(s)$ .

## III. COMPUTATIONAL DETAILS

The computational details are mostly identical those in Ref. [32]. Our calculations were based on the QUANTUM ESPRESSO (QE) package<sup>58</sup> with PBE ultrasoft pseudopotentials designed by Garrity, Bennett, Rabe, and Vanderbilt (GBRV).<sup>59</sup> Where applicable, all systems were structurally optimized with a wave-function cutoff of 50 Ryd and a density cutoff of 600 Rvd. The energy convergence criterion was  $1 \times 10^{-8}$  Ryd and the force convergence criterion was  $1 \times 10^{-6}$  Ryd/Bohr. Calculations on molecular dimers/monomers were performed in boxes with at least 15 Å of vacuum for padding. Layered structures were obtained from the Inorganic Crystal Structure Database (ICSD) and we used the procedure in Refs. [60–62] to optimize those systems, i.e. we relaxed the inter-layer c-axis with  $12 \times 12 \times 6$  k-points and kept the a-lattice constant at the experimental value. Single layers were calculated with fixed a-lattice constant and with at least 12 Å vacuum along the c-axis, utilizing a  $12 \times 12 \times 1$  k-mesh. The structure of the molecular crystals for the X23 dataset were obtained from Ref. [63] and all structural degrees of freedom were optimized, sampling only the  $\Gamma$ -point of the Brillouin zone. Finally, for the adsorption of benzene on the (111) surface of the coinage metals Cu, Ag, and, Au we used 6 atomic metal layers<sup>64</sup> of which we kept the three bottom layers fixed; we used 9 Å vacuum and a  $4 \times 4 \times 1$  k-mesh.

While the physical aspects of all systems are well converged with the kinetic energy cutoffs provided above,

plots of  $\Delta e_{\rm gx}(s)$  from Eq. (4) are very noisy due to the finite spatial integration grid in plane-wave calculations used for  $n(\mathbf{r})$  and  $s(\mathbf{r})$  in Eq. (5). While increasing the energy cutoff results in a denser grid, it only provides diminishing returns for noise reduction; we explored density cutoffs up to 1920 Ryd. To limit the grid sensitivity, we introduced broadening by first integrating  $\Delta e_{\rm gx}$ 

$$\Delta E_{\rm gx}(s) \approx \int_0^\infty ds' \ \Delta e_{\rm gx}(s') \ G(s, s') \ ,$$
 (8)

where

$$G(s, s') = \frac{1}{e^{(s'-s)/\beta} + 1}$$
 (9)

is a Fermi-type function, and then calculated the numerical derivative to arrive at a broadened  $\Delta e_{\rm gx}(s)$ . This procedure drastically reduces the gird-sensitivity. We found that small values of  $\beta=0.03$  are sufficient. However, even with this approach some systems required density cutoffs as high as 1920 Ryd to ensure low noise in  $\Delta e_{\rm gx}(s)$ .

In addition to  $\Delta e_{\rm gx}(s)$  and  $\Delta E_{\rm gx}(s)$ , we calculate the s-resolved exchange force  $\Delta k_{\rm gx}(s)$  from Eq. (7) through a finite difference method wherein we calculate  $\Delta e_{\rm gx}(s)$  for two different distances. For example, for the benzene dimer, we move the "frozen" monomers along the natural direction defined by the S22×5<sup>65</sup> dataset by 0.05 Å.

### IV. RESULTS

#### A. The Benzene Dimer

Figure 2 provides a detailed s-analysis of one representative van der Waals-bound dimer, i.e. the benzene dimer in  $C_{2h}$  configuration, which is part of the commonly studied S22×5 set of molecular dimers. The center of Fig. 2 shows the s-resolved exchange interaction energy  $\Delta e_{\rm gx}(s)$  of the benzene dimer for the optimal "1.0" CCSD(T) separation. Unless otherwise noted, all such curves are generated with the GGA exchange of DF3-opt1. The curve has a negative regime at low s, contributing in an attractive way to binding, and a positive regime at higher values of s, contributing in a repulsive way. The various motifs in Fig. 2 show iso-surfaces of the benzene dimer at different values of s. These can be linked to the shape of  $\Delta e_{\rm gx}(s)$  and the different spatial regions contributing to it. For clarity, the adjacent

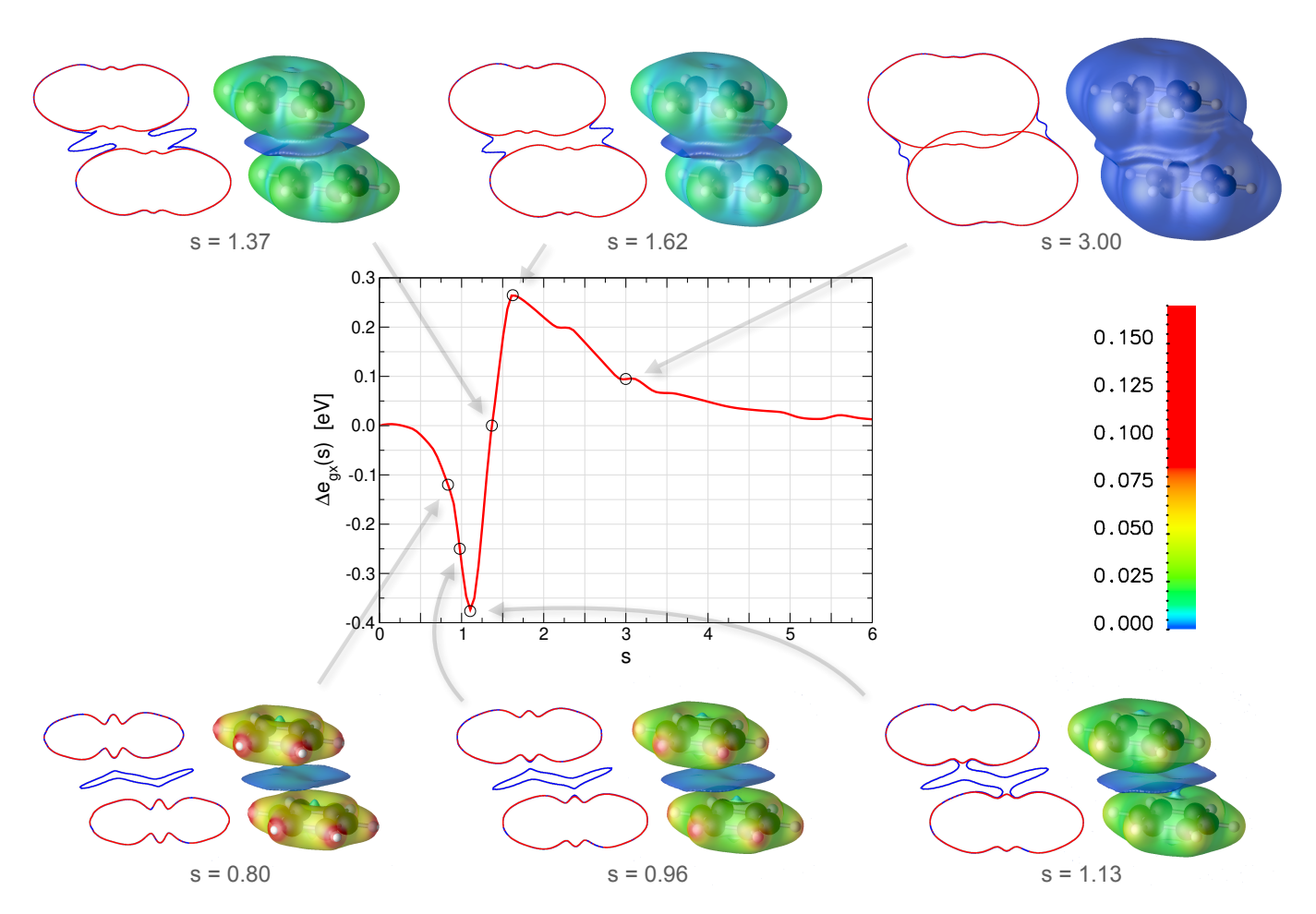


FIG. 2. (center) s-resolved exchange interaction energy  $\Delta e_{\rm gx}(s)$  for the benzene dimer in  ${\rm C}_{2h}$  configuration for the optimal CCSD(T) separation, calculated with DF3-opt1. (top and bottom insets) Iso-surfaces for different values of s. The electronic charge density is mapped onto the iso-surface in color and can be read off the color bar in units of  $e/{\rm Bohr}^3$ . Each iso-surface is further mapped onto a plane that goes through the center of the dimer, resulting in iso-lines; lines of the dimer are blue and lines of the individual monomers are red.

blue iso-lines show intersections of the dimer iso-surfaces with a plane crossing the center of the dimers, overlaid by red iso-lines corresponding to individual monomers. Consider first the attractive low-s regime. For s=0.80 and s=0.96, three distinct surfaces are apparent: two surrounding the individual monomers and one disk-shaped surface in-between them. For these s values, the iso-surfaces of the monomers are nearly identical to the corresponding portions of the dimer iso-surface. Thus, for these low-s values, there is a near-perfect cancellation of the contributions of these surfaces to  $\Delta e_{\rm gx}(s)$  in Eq. (4) and the attractive energy therefore comes almost exclusively from the disk region.

As the iso-surfaces grow with increasing s, they eventually start overlapping and merging. At s=1.13, the onset of this merger has begun, as evident in the isolines. The merger causes both the disk and molecular iso-surfaces to effectively loose surface area. This reduces the attractive contributions from the disk and gives rise to repulsive contributions to the s-resolved exchange energy due to less and less cancellation of the monomer

iso-surfaces. This merging thus causes the crossover from negative to positive  $\Delta e_{\rm gx}(s)$ . Once the merger has completed, the overall shape of the combined dimer iso-surface remains similiar while growing outwards around the benzene dimer. As the s iso-surface grows, the charge density decrease, which is the cause for the decrease in  $\Delta e_{\rm gx}(s)$  beyond the positive peak at s=1.62. In Fig. S1 in the Supplementary Information (SI), we provide a s-n scatter-plot,  $^{38,39}$  which complements this analysis.

In Fig. 3, we show  $\Delta e_{\rm gx}(s)$  for the five separations defined in the S22×5 dataset, from 0.9 to 1.0, 1.2, 1.5, and 2.0 times the optimal CCSD(T) binding separation. The crossover and ranges spanned by the attractive and repulsive regimes vary significantly with respect to separation, but the overall shapes of the curves remain quite similar. The analysis of the benzene dimer at optimal separation allows us to also interpret the change in  $\Delta e_{\rm gx}(s)$  with separation. On the one hand, the onset of the merger in s increases with separation, as the central disk has more room to grow before merging, causing the shift in  $\Delta e_{\rm gx}(s)$  to larger s values with increasing separation. On

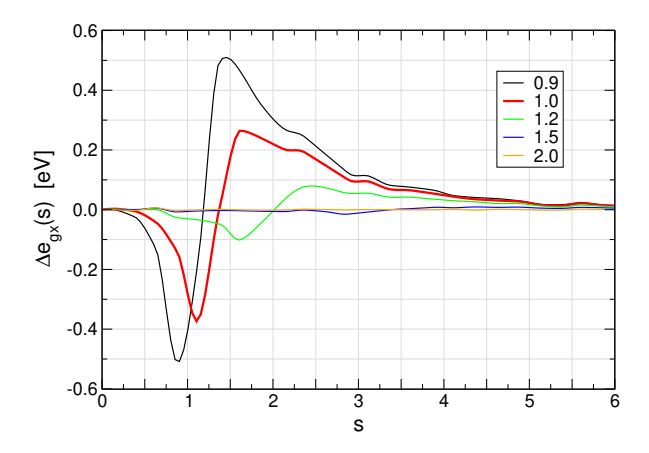


FIG. 3. s-resolved exchange interaction energy  $\Delta e_{\rm gx}(s)$  for the benzene dimer in  ${\rm C}_{2h}$  configuration for separations ranging from 0.9 to 1.0, 1.2, 1.5, and 2.0 times the optimal CCSD(T) binding separation, as defined in the S22×5 dataset.<sup>65</sup>

the other hand, the decrease in magnitude of  $\Delta e_{\rm gx}(s)$  with increasing separation can be explained by the lower electronic densities in the inter-molecular region.

## B. Comparison of Exchange Functionals at Optimal Separation

Table I shows the total interaction energy  $\Delta E$  of the benzene dimer at the "1.0" separation, the corresponding gradient exchange portion  $\Delta E_{\rm gx}(\infty)$ , the non-local correlation contribution  $\Delta E_{\rm c}^{\rm nl}$ , the gradient exchange portion of the force  $\Delta K_{\rm gx}(\infty)$ , and the dimer distance resulting from a full optimization for various vdW-DF functionals. Comparison with CCSD(T) reference values shows that the performance of the different functionals can vary significantly. Trends in the interaction energy  $\Delta E$  can be related to  $\Delta E_{\rm gx}(\infty)$ —taking the differences in  $\Delta E_c^{\rm nl}$  into account—which in turn can be related to  $\Delta e_{\rm gx}(s)$  (top panel of Fig. 4) and  $F_{\rm x}(s)$  (top panel of Fig. 1). The optimized binding distances are related to forces  $\Delta k_{\rm gx}(s)$  (bottom panel of Fig. 4), which can be related to  $\mathrm{d}F_{\rm x}(s)/\mathrm{d}s$  (bottom panel of Fig. 1).

When integrating  $\Delta e_{\rm gx}(s)$  to get  $\Delta E_{\rm gx}(s)$  in Fig. 4, at some point the negative and positive contributions of  $\Delta e_{\rm gx}(s)$  cancel, causing  $\Delta E_{\rm gx}(s)$  to cross the zero line. Since  $F_{\rm x}(s)$  varies quite slowly with s, this crossing occurs at quite similar values of s for most functionals (in the case of the benzene dimer at  $s \approx 2$ ). All net contributions to  $\Delta E_{\rm gx}(\infty)$  are therefore given by the shape of  $F_{\rm x}(s)$  beyond this crossing point. However, even small differences in the crossing point—or correspondingly the value of  $\Delta E_{\rm gx}(s=2)$ —do matter, since the  $\Delta e_{\rm gx}(s)$  curve is so steep in this region, making the values of  $F_{\rm x}(s)$  below this crossing point also important. Here, we discuss differences in  $\Delta E_{\rm gx}(\infty)$  caused by different  $F_{\rm x}(s)$  in terms of contributions of negative and positive regions in  $\Delta e_{\rm gx}(s)$ ,

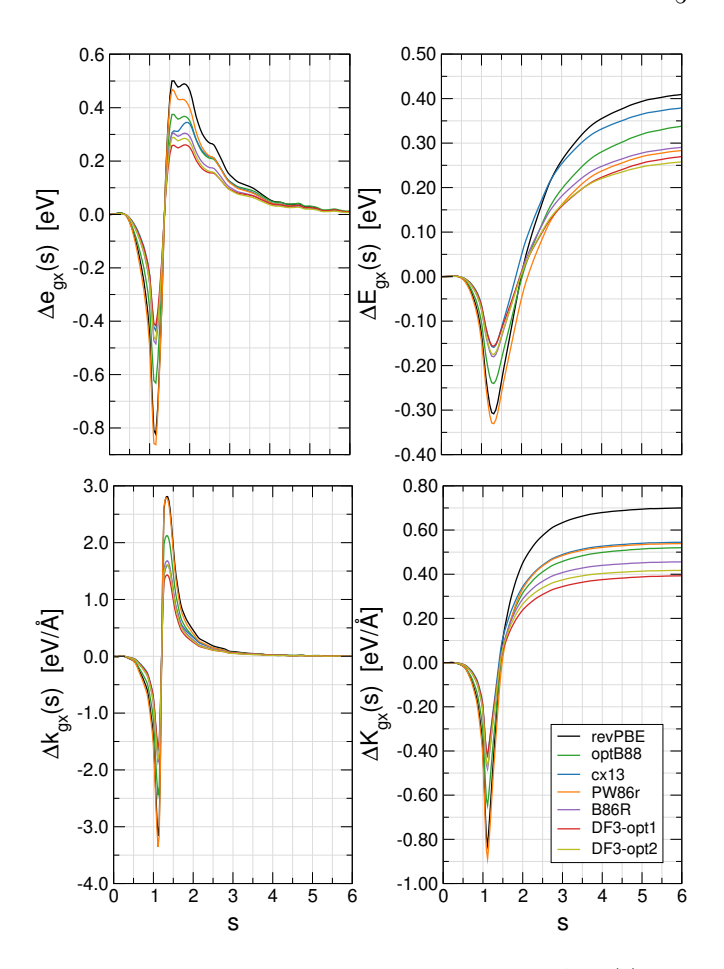


FIG. 4. s-resolved exchange interaction energy  $\Delta e_{\rm gx}(s)$ , exchange energy  $\Delta E_{\rm gx}(s)$ , s-resolved exchange force  $\Delta k_{\rm gx}(s)$ , and exchange force  $\Delta K_{\rm gx}(s)$  for the benzene dimer in  ${\rm C}_{2h}$  configuration for several different exchange functionals. Further analysis can be found in Fig. S2 in the SI.

but one could alternatively analyze it in terms of shifts in crossing points of  $\Delta E_{\rm gx}(s)$  and the values of  $F_{\rm x}(s)$  beyond that. Such an analysis is provided in Fig. S2 in the SI.

We now discuss how specific shapes of  $F_{x}(s)$  and  $\Delta e_{\rm gx}(s)$  give rise to different values of  $\Delta E_{\rm gx}(\infty)$ . We first compare PW86r, DF3-opt2, and B86R. These have quite similar  $\Delta E_{\rm gx}(\infty)$ , but the  $F_{\rm x}(s)$  values of PW86r are consistently larger than those of DF3-opt2 and B86R. However, since those larger values partially cancel through negative and positive contributions of  $\Delta e_{\rm gx}(s)$ , the end result is quite similar values of  $\Delta E_{\rm gx}(\infty)$ . The slightly lower values of DF3-opt2 compared to B86R can be related to the smaller values of  $F_{\rm x}(s)$  for large s. Comparing cx13 and PW86r gives a different weighing. On the one hand,  $F_{\rm x}(s)$  of cx13 is lower than that of PW86r (as is B86R) in the attractive regime, but on the other hand, at larger s,  $F_{\rm x}(s)$  becomes more similar until they become identical at large  $s.^{67}$  cx13 therefore has a significantly reduced attractive portion of the exchange compared to PW86r, but retains quite similar repulsive contributions, resulting in significantly larger  $\Delta E_{\rm gx}(\infty)$ . This analy-

TABLE I. Total interaction energy  $\Delta E$  of the benzene dimer in  $C_{2h}$  configuration at the optimal CCSD(T) distance [eV], corresponding gradient exchange portion  $\Delta E_{\rm gx}(\infty)$  [eV], non-local correlation contribution  $\Delta E_c^{\rm nl}$  [eV], gradient exchange portion of the force  $\Delta K_{\rm gx}(\infty)$  [eV/Å], and dimer distance [Å] resulting from a full optimization. CCSD(T) results are given for reference.<sup>65,70</sup>

Functional	reference	DF1	DF2	DF1-optB88	DF1-cx	DF2-B86R	DF3-opt1	DF3-opt2
Exchange	_	${\rm revPBE}$	PW86r	optB88	cx13	B86R	$\mathrm{DF}3\text{-}\mathrm{opt}1$	$\mathrm{DF3} ext{-}\mathrm{opt2}$
$\Delta E \text{ [eV]}$	-0.1219	-0.0881	-0.0968	-0.1416	-0.1120	-0.0937	-0.1191	-0.1234
$\Delta E_{\rm gx}(\infty) \ [{\rm eV}]$		0.4281	0.3056	0.3626	0.3891	0.3094	0.2990	0.2783
$\Delta E_{ m c}^{ m nl} \; [{ m eV}]$		-0.3879	-0.2865	-0.3980	-0.3969	-0.2923	-0.3090	-0.2891
$\Delta K_{\mathrm{gx}}(\infty) \; [\mathrm{eV/Å}]$	_	0.6998	0.5389	0.5203	0.5449	0.4561	0.3930	0.4175
Distance [Å]	3.765	4.214	4.064	3.939	4.089	3.989	3.864	3.914

sis shows how PW86r and B86R, both with guite different  $F_{\mathbf{x}}(s)$ , can give quite similar energies when combined with DF2 non-local correlation. cx13 with its much larger value of the exchange energy is comparable with DF1, which has a much larger negative non-local correlation energy contribution to the binding. Similar to PW86r, revPBE has quite large values of  $F_{x}(s)$  in the attractive regimes, but more than compensates for this by having even larger values of  $F_{\mathbf{x}}(s)$  than the other functionals in most of the repulsive regime, with the end result of a too low interaction energy even when combined with DF1 non-local correlation. For most values of s, optB88 falls somewhere in-between cx13 and revPBE, making it a suited companion to DF1 non-local correlation, which is what it was fitted to.66 However, since optB88 in the repulsive regime is closer to cx13 than revPBE, it has a lower exchange energy than cx13 and DF1-optB88 overestimates the full interaction energy for this system.

Looking at the forces, we find that the slope of the enhancement factor at typical s values plays a significant role. In the lower panels of Fig. 4 we see how the s-resolved force  $\Delta k_{\rm gx}(s)$  crosses zero at  $s_0^{\Delta k}=1.21$  and  $\Delta K_{\rm gx}(s)$  crosses zero at almost precisely  $s_0^{\Delta K}=1.45$ , which is also approximately the location of the upward peak in  $\Delta e_{\rm gx}(s)$ . The force curves are much more narrow and localized than the corresponding s-resolved exchange energy curves. Because they are so narrow and the negative and positive regions partially cancel, the slope of  $\mathrm{d}F_{\mathrm{x}}/\mathrm{d}s$  around  $s_0^{\Delta k}$  becomes very important for analysis, since it effectively determines the weighing of the relative negative and positive portions. Moreover, typical  $dF_{x}/ds$  differ more from each other than typical  $F_{x}(s)$  in this regime. In fact, comparing Fig. 1 and Table I and the lower left panel of Fig 4, we observe a strong correlation between  $dF_x/ds(s_0^{\Delta k})$  and the total exchange force for each functional. The ordering from largestto-smallest  $dF_x/ds(s_0^{\Delta k})$ —i.e. revPBE, cx13  $\approx$  PW86r, optB88, B86R, DF3-opt2, and DF3-opt1—matches the ordering of  $\Delta K_{\rm gx}(\infty)$ .

This ordering can also be connected to the differences in binding separations in Table I, which in a first-order approximation is proportional to the differences in the exchange force for the same non-local correlation. Even for the cases where the non-local correlation differs the comparison has merit as the non-local correlation has a slower distance dependence than the exchange. Thus, the trend in  $dF_x/ds(s_0^{\Delta k})$  explains why standard DF1 with revPBE has the largest binding distance and DF3-opt1 has the shortest. The only exception is the somewhat larger separation of DF2-B86R compared to DF1-optB88, which can be attributed to the smaller attractive force of DF2 non-local correlation compared to DF1.

The fact that differences in forces can be attributed to a rather narrow region of  ${\rm d}F_{\rm x}/{\rm d}s$  and somewhat lower values of s compared to differences in energies, explains why updating the exchange of DF1 to that of e.g. optB88 and cx13 had the capability to improve both binding energies and distances, and likewise for the switch from PW86r to B86R for DF2. However, as shown in Fig. 3, the typical s values shift with separation and good performance at binding separations is no guarantee that the interaction energies beyond the binding separation is accurate for a given non-local correlation functional. In fact, inaccurate interaction energies beyond the binding separation were one of the key motivations for developing vdW-DF3. $^{32}$ 

#### C. S22×5 Dataset at Optimal Separation

We next analyze the s-resolved exchange interaction energy  $\Delta e_{\rm gx}(s)$  (upper panel of Fig. 5) and force  $\Delta k_{\rm gx}(s)$ (lower panel for Fig. 5) for the 22 dimers in the  $S22 \times 5$  set at the "1.0" separation. 65 In general, the iso-surfaces for these dimers exhibit the same main features as for the benzene dimer, i.e. the formation of a disk in-between the molecules at low-s values, a merger process, and subsequent iso-surface growth. The similar shapes of the  $\Delta e_{\rm gx}(s)$  curves compared to the benzene dimer (system 11) is reflected in the statistical representation in the upper panel. The blue band indicates the domain that covers 80% of the negative part of the curve, centered around the median (blue curve). The wider red band is the corresponding data for the positive curve; the much larger domain above the median (red curve) reflects the longer tails of the  $\Delta e_{\rm gx}(s)$  curves. The black curve indicates  $s_0^{\Delta e}$ , i.e. the point where  $\Delta e_{\rm gx}(s)$  crosses zero.

A number of trends can be seen from Fig. 5. Compar-

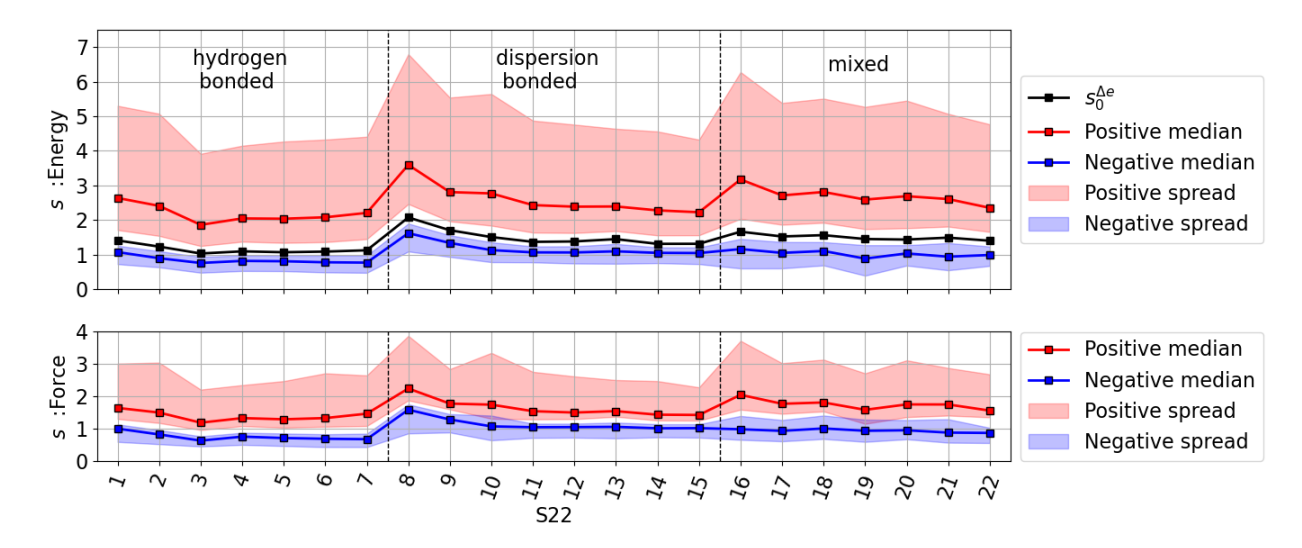


FIG. 5. Statistical data for the S22 dataset of molecular dimers. For full  $\Delta e_{\rm gx}(s)$  curves and for dimer numbering see Fig. S3. The median and spread for each dimer are calculated separately for the positive and negative regions of  $\Delta e_{\rm gx}(s)$  and  $\Delta k_{\rm gx}(s)$ , see Fig. S4 for details.

ing the hydrogen-bonded and dispersion-dominated systems, the average  $s_0^{\Delta e}$  value increases from 1.15 to 1.51, with similar shifts in magnitude for the medians. For systems involving the smallest molecules and in which hydrogen atoms are involved in the binding, the typical  $s_0^{\Delta e}$  value is shifted to larger values, which is particularly evident for the methane dimer (system 8,  $s_0^{\Delta e} = 2.1$ ) and the ethene-ethyne dimer in the T-configuration (system 16,  $s_0^{\Delta e} = 1.7$ ). For some of the mixed systems and dispersion-bonded systems, the iso-surfaces have several merging points at different values of s, resulting in more wiggled  $\Delta e_{\rm gx}(s)$  curves. This is reflected in the broader blue bands for the mixed systems than for the hydrogenand dispersion-bonded systems.

As for the benzene dimer (see Fig. 4), the force bands are noticeably narrower than the energy bands and shifted to lower s-values; for instance the negative median is shifted from an average of 1.25 to 0.96. An added complication for the force curves is that for systems with more complicated iso-surface mergers, this can cause rapid oscillations in  $\Delta k_{\rm gx}(s)$ . The exact  $s_0^{\Delta k}$  roots of these curves can be hard to disentangle and depend on broadening choices in Eq. (9) and therefore are not shown. These oscillations are also the reason why some of the blue and red bands partially overlap in the lower panel of Fig. 5.

As for the benzene dimer, trends in the curves for the entire  $S22\times 5$  set at the "1.0" separation (provided in Fig. S3) can be compared with Fig. 4. In line with the analysis for the benzene dimer, such a comparison suggests that more local changes in  $F_{\mathbf{x}}(s)$  in Fig. 1 may allow for targeted improvements, in particular for the binding separations. Such modifications could potentially overcome the competing requirements uncovered in Ref. [32]. Our results can for instance explain why DF1-cx significantly overestimates the methane dimer binding separa-

tion (system 8, by 0.25 Å) compared to an almost perfect agreement with the reference data for DF3-opt1 (see Table S1 in the SI). As seen in the lower panel of Fig. 5, the crossing region between the blue and red bands around  $s \approx 1.6-1.8$  coincides with the region in which  $\mathrm{d}F_\mathrm{x}/\mathrm{d}s$  values of cx13 become larger than those of revPBE (DF1 overestimates this dimer distance by 0.175 Å). DF3-opt2 is the only functional underestimating the separation of this dimer (-0.02 Å) and also has the lowest  $\mathrm{d}F_\mathrm{x}/\mathrm{d}s$  in this region, whereas DF3-opt1 with slightly larger  $\mathrm{d}F_\mathrm{x}/\mathrm{d}s$  in this region, has a perfect agreement with the reference data.

The precise reason why a functional like DF1-cx can give fairly accurate binding energies for the benzene dimer (see Tables S2 and S3) while having an initially slow increase in  $F_{\rm x}(s)$ —which is why the functional provides excellent lattice constants of covalent solids—is the increase to larger  $F_{\rm x}(s)$  starting at  $s\approx 1.5$ . Without this increase, the repulsive components are not sufficiently weighted to counteract the large energetic contribution from the non-local correlation of DF1. In the case of DFcx,  $dF_{x}(s)/ds$  is particularly large around  $s \approx 2$ , which is significantly beyond the crossing points of most of the dimers, but not the smallest ones. Thus, our analysis indicates that it is not possible to design very accurate and broadly applicable functionals by tuning the GGA exchange as long as one relies on DF1 non-local correlation.

## D. Layered Structures

Next, we analyze the reduced-gradient for a set of nine layered structures, a subset of systems that has been used in several other studies. <sup>32,61,62,72</sup> First, we focus on graphite as a representative case within this subset. Fig-

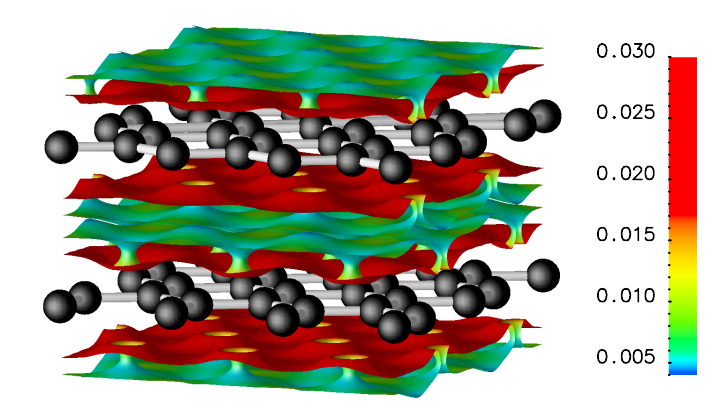


FIG. 6. Iso-surface of s=1.0 for a graphite supercell; electronic charge density in units of  $e/\mathrm{Bohr}^3$  is mapped onto the iso-surface. Along the edge one can see cut-open "tunnels" connecting individual surfaces, showing the beginning of a merger that gradually depletes attractive interaction energy in the system.

ure 6 shows the iso-surface of s=1.0 for a graphite supercell with charge-density mapping. As for the benzene dimer, there are two types of iso-surface to consider: the "monomer" iso-surfaces that grow around the individual layers and the "disk", which is here more like a "sheet", that represents the interaction between adjacent layers.

In parallel to the benzene dimer, at very low-s values the iso-surfaces formed around the individual layers are almost identical to those of graphene sheets, so that these low-s iso-surfaces cancel out and only the interlayer sheet contributes to the interaction energy. As we move to higher s, the iso-surfaces grow outward from their planes of origin. By s = 1.0, as shown in Fig. 6, the iso-surfaces have expanded to the point that they begin to merge with one another through spatially periodic "tunnels". In the benzene-dimer case this merger corresponds to immediate losses in attractive energy. For graphite, however, the parts of the inter-layer sheet that have not been "annihilated" continue to grow in the direction of the carbon atoms, increasing the charge density on that iso-surface. It is this increase in charge density that temporarily offsets the decrease in surface area. The loss in surface area does not begin to dominate until s = 1.17, which is the downward peak of graphite's  $\Delta e_{\rm gx}(s)$ , as shown in the red curve in Fig. 7. After this point, the inter-layer iso-surface is gradually "annihilated" along with the monolayer iso-surfaces in the dimer, resulting in a shift from negative energy (attraction) to positive energy (repulsion). By s = 1.31, the location of graphite's upward peak in  $\Delta e_{\rm gx}(s)$ , the isosurfaces in graphite completely vanish. This means that any contribution to the interaction energy above that svalue is repulsive and entirely dependent on the energy of a single graphene layer.

Though we use graphite as our main example, the same iso-surface behavior is true of all of our layered systems. This is demonstrated by the fact that they all have the

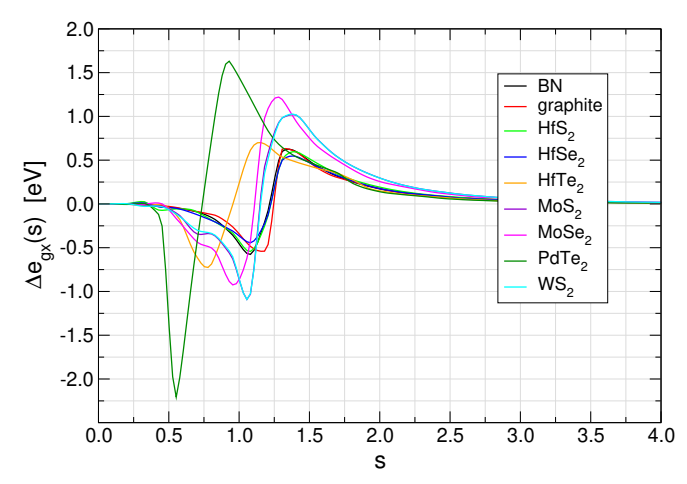


FIG. 7. s-resolved exchange interaction energy  $\Delta e_{\rm gx}(s)$  for a set of nine layered systems.

same overall shape of  $\Delta e_{\rm gx}(s)$ , see Fig. 7: an attractive contribution to interaction energy at low s, followed by a sharp transition to repulsive energy at higher s, and then a regression to zero exchange interaction energy after the full layered system no longer contributes to the interaction. This regression is due to the decrease in charge density as iso-surfaces of s grow more distant from the monolayer. We find that all layered structures abide by this sequence with only slight variations between individual types of systems, but there are some clear differences in the relevant value of s. PdTe<sub>2</sub>, in particular, has a  $\Delta e_{\rm gx}(s)$  curve that is shifted to the left compared to the other systems, also evident in the statistical data provided in Fig. 8. This shift is caused by the partly covalent character of this inter-layer binding, evidenced by the sizable GGA-level binding energy found in e.g. Ref. [73]. This results in the shortest distance between any inter-planar atoms in all of our layered structures. Thus, the "disk" iso-surface that arises between the tellurium atoms has less space to grow, resulting in less contribution from higher-s values. We also see that certain systems such as MoS<sub>2</sub>, MoSe<sub>2</sub>, and WS<sub>2</sub> have a tendency for their  $\Delta e_{\rm gx}(s)$  to plateau slightly before hitting peak attraction. We believe that this is due to asymmetry in the iso-surfaces, where parts of the interplanar disk merge with the monolayer iso-surfaces long before the remainder does. This results in a brief and small repulsive contribution even as the attractive energy continues to build.

It is instructive to compare the shifts in  $\Delta e_{\rm gx}(s)$  with the predicted inter-layer separations in Table S4 and the form of  ${\rm d}F_{\rm x}/{\rm d}s$  for different functionals. In particular, DF2 has notoriously inaccurate interlayer separations for some systems;  $^{30,67,73}$  in the case of PdTe<sub>2</sub> by as much as 0.9 Å, while for HfTe<sub>2</sub> and MoSe<sub>2</sub> by approximately 0.6 Å. WS<sub>2</sub>, HfSe<sub>2</sub>, and MoS<sub>2</sub> have similar curves and DF2 overestimates their separation by 0.4 Å. Graphite, BN, and HfS<sub>2</sub> also have similar curves and DF2 overestimates their separation by approximately 0.15 Å. For

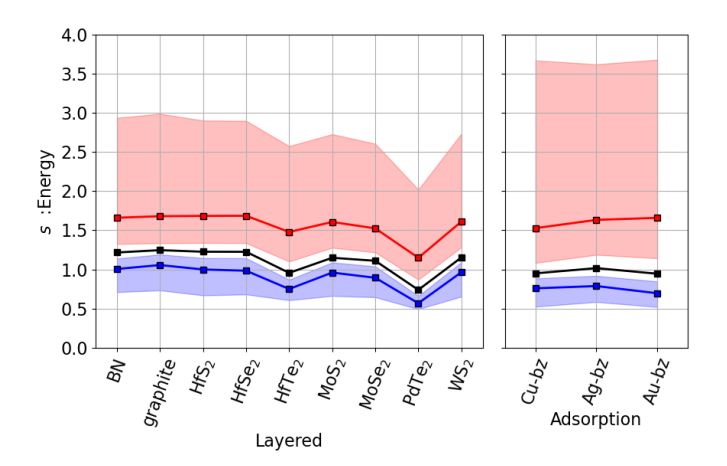


FIG. 8. Statistical analysis of  $\Delta e_{\rm gx}(s)$  for (left) nine layered systems and (right) benzene adsorbed on three surfaces. See legend in Fig. 5 for more details.

these three, DF1 has somewhat larger overestimation of inter-layer separations, i.e. by 0.2 Å. The trends in binding separation can be linked to the much larger  $\mathrm{d}F_\mathrm{x}/\mathrm{d}s$  of PW86r for  $s\approx 0.2$  to  $s\approx 0.8$  used in DF2, compared to all others, while the regions for which DF1 gives larger separations can be linked to the crossing of  $\mathrm{d}F_\mathrm{x}/\mathrm{d}s$  for PW86r and revPBE at  $s\approx 1$ . Trends in inter-layered binding energies are harder to distinguish, since the separations are influenced by the functional. However, we can infer that the overall more accurate energies of DF1-cx compared to DF1-optB88 can be linked to the larger  $F_\mathrm{x}(s)$  for smaller s and similar magnitude for larger s, causing the exchange attraction to be weighted more for optB88 and thus resulting in larger binding energy overestimation.

Finally, we give attention to the fact that all vdW-DFs with accurate inter-layer separation overestimate the binding energy of layered systems as seen in Table S4. with DF3-opt1 being the best performing with a MARD of 13.55%. While improving this may require updating the non-local correlation further, it is interesting to analyze the role of the exchange energy compared to the molecular dimers. While being a quite accurate functional for the energies at the "1.0" separation for the S22×5 set in Table S3, optB88 is the worst performing for the energies of layered systems (MARD of 32.36%). If we disregard revPBE and PW86r (as DF1 and DF2 have inaccurate inter-layer separations), optB88 has the largest  $F_{\mathbf{x}}(s)$  among the functionals beyond s=2.9. In this tail region, optB88 picks up significant repulsive contributions for the molecular dimers, while for layered systems this tail region has almost vanished, clearly evident by comparing Fig. 5 and Fig. 8.

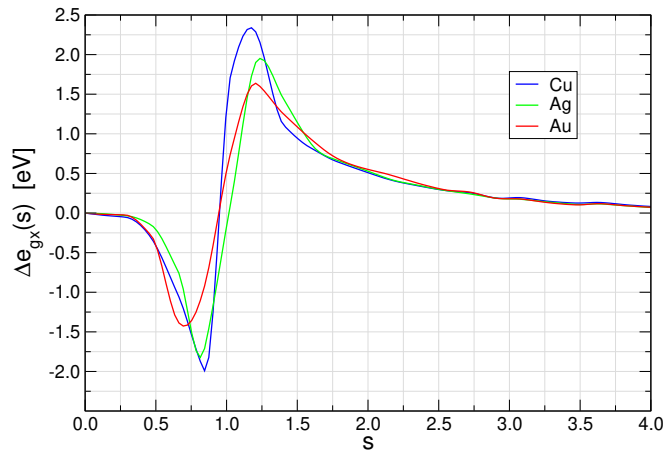


FIG. 9.  $\Delta e_{\rm gx}(s)$  for benzene adsorbed on the coinage metals Cu, Ag, and Au.

## E. Benzene Adsorption on Cu/Ag/Au (111)

Molecular adsorption on coinage metals has traditionally been a challenging problem to model with DFT methods<sup>52</sup> due to very distinct properties of the surface and the molecule as well as different response properties of the surface and bulk regions of the metal. Here, we study the adsorption of benzene on the (111) surface of Cu, Ag, and Au and analyze the s dependence. Figure 9 shows the profile of  $\Delta e_{\rm gx}(s)$  for these three cases; corresponding statistical properties of the domains are indicated in the right panel of Fig. 8. Moreover, Fig. 10 shows the iso-surfaces of s for benzene on Ag (111) as a representative system. As for the other systems, we find that the iso-surfaces growth and merger dictates the dependence of the exchange interaction energy on s. The first iso-surface is at s = 0.50, which is below the 80% negative domain (see Fig. 8). We observe three distinct types of surfaces: ones surrounding and intrinsic to the benzene molecule, ones permeating and surrounding the Ag lattice, and a single, very-low charge-density surface directly between the benzene and metal surface. As the iso-value of s grows, so too does the interaction iso-surface until it runs out of space and begins to "annihilate" on contact with the benzene and Ag iso-surfaces. The lower panel of Fig. 10 shows the iso-surface for s = 0.84, i.e. the location of the negative peak in  $\Delta e_{\rm gx}(s)$  for this system. Here, the interaction iso-surface has been partially "annihilated" on the side facing the Ag atoms and is just beginning to merge with the benzene molecule as well. As this merger progresses, the interaction iso-surface loses surface area and charge density, leaving the energies of the isolated benzene and Ag surfaces to dominate the interaction. This results in the permanent transition to repulsive exchange interaction energy that we see around  $s \approx 1.0$ .

The dissimilarity between the benzene molecule and metal surface makes this system interesting to compare with the molecular dimers and layered systems. The neg-

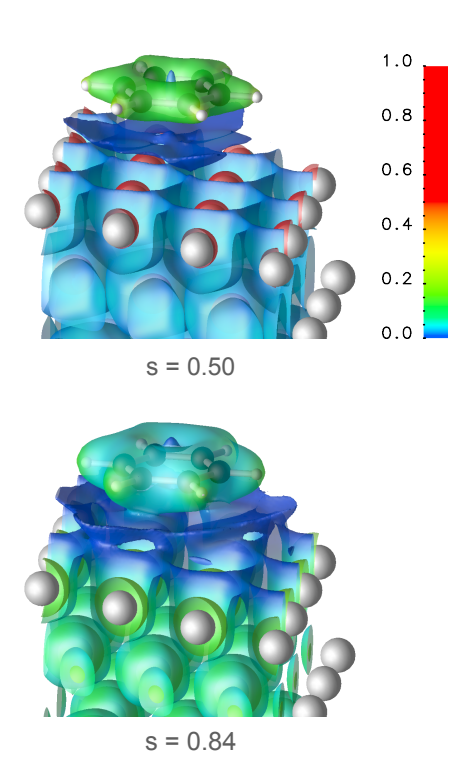


FIG. 10. Iso-surface of s = 0.50 and s = 0.84 for benzene adsorbed on the Ag (111) surface. The electronic charge density in units of  $e/\text{Bohr}^3$  is mapped onto the iso-surface.

ative parts of the curves in Fig. 9 have an onset at lower values of s, almost as low as for PdTe<sub>2</sub>, in particular for Au. The localization and negative/positive peak magnitude can also be ranked as Cu > Ag > Au. For the negative region, the surface adsorption peaks are more localized than the ones for layered systems, while for the positive region they are much broader, see Fig. 8. The shift to lower-s values and localization on the negative side can be understood from the asymmetry of the "annihilation" of the molecule and metal-surface iso-surfaces; the broadening on the positive side arises from the distinctness of the individual surfaces and that of benzene. We further note that benzene on Ag (111) exhibits a shifting to larger-s values on the positive side and a slight broadening compared to the Cu case, while for Au (111) we only see broadening. This slight shift in trend is a testament to the distinct electronic properties of these surfaces and might be related to the lower binding energy on Ag (111), a trend only DF1-cx gets right among the functionals, see Table S5. Finally, all the  $\Delta e_{gx}(s)$ curves have very similar large-s behavior, which is primarily due to the benzene monomer contributions.

#### F. Molecular Crystals

Finally, our reduced-gradient analysis was also done for the X23 dataset of molecular crystals. Figure 11 shows the statistical analysis of  $\Delta e_{\rm gx}(s)$  for the full dataset

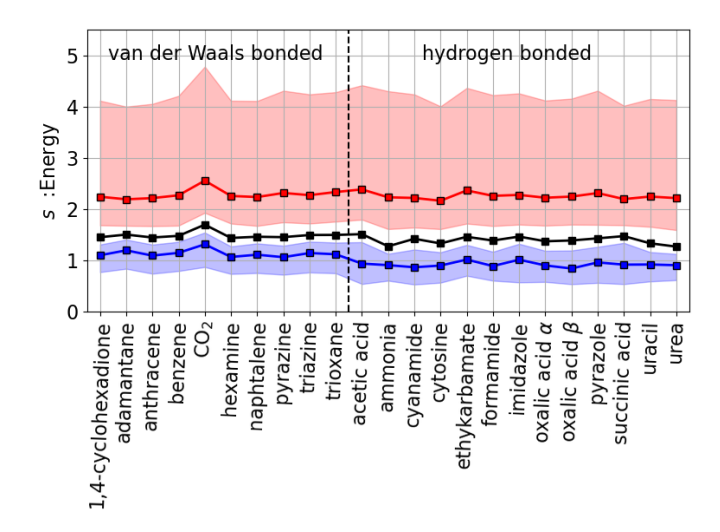


FIG. 11. s-resolved exchange interaction energy  $\Delta e_{\rm gx}(s)$  for the X23 dataset of molecular crystals.<sup>74</sup> See legend in Fig. 5 for more details.

and the individual curves are provided in Fig. S5 in the SI. Among these systems we find a high degree of similarity and no particular structure to serve as a representative. Nonetheless, the mechanism behind their interactions can still be described similar to the benzene dimer. However, whereas the benzene dimer features a single interacting iso-surface between the two molecules, we see several iso-surfaces between adjacent molecules in the molecular crystals. And, due to differences in orientation of the molecules relative to one another, we find that the iso-surfaces residing between them take a variety of different shapes and sizes. Still, the same mechanisms of how these iso-surfaces contribute to the s-resolved exchange interaction energy come into effect: At low s, iso-surfaces form around and in-between atoms, with the ones in-between causing exchange attraction. In the case of the X23 dataset, the crossing point from positive to negative values occurs on average at  $s_0^{\Delta e} = 1.44$ , with the negative and positive medians on average at 1.01 and 2.27.

Comparing the statistical data for molecular dimers in Fig. 5 with those of molecular crystals in Fig. 11, we speculate that the crystals are more similar to each other than the dimers. This might be due to the stronger attractive dispersion forces arising due to the three-dimensional geometry in crystals, which compresses some of the most weakly bonded systems—but, the effect is smaller for crystals made out of larger molecules since the effect of the three-dimensional geometry is smaller. In effect, the effective packing distances in terms of the s iso-surfaces become more similar. In turn, this analysis suggests that it could be possible to design functionals that provide accurate performance for all molecular crystals in the X23 data set at the same time.

Comparing molecular crystals with molecular dimers and layered systems (Figs. 5, 8, and 11), it becomes evident that the exchange interaction of molecular crystals is more similar to molecular dimers than layered systems including graphite. A consequence of this is that DF2 on one hand can provide accurate volumes of molecular crystals, but on the other severely overestimates separations of layered systems, whereas DF1-cx is accurate for both (see Tables S4 and S6). This can be related to their crossing of d $F_{\rm x}/{\rm d}s$  at s=1.34, i.e. slightly below  $s_0^{\Delta e}=1.44$ , which is a good match considering the shift in s-resolved exchange interaction energy and forces in Fig. 4.

#### V. CONCLUSIONS

Our study provides a thorough analysis of reducedgradient values, their spatial distribution, and how they contribute to the exchange component of the binding of a variety of different van der Waals complexes. We find that attractive contributions to the exchange interaction energy can be attributed to low-density regions between the constituents with disk-like iso-surfaces. We further identify a mechanism wherein the surface area of these disks decreases through merging with other iso-surfaces and switches the gradient-correction to exchange from attractive to repulsive. Our analysis shows that there are clear differences in the reduced-gradient resolved exchange interaction energy for different classes of van der Waals complexes. Analyzing these differences provides a way to explain why different exchange functionals used in vdW-DF perform differently for different classes of systems. In turn, this can provide valuable guidance for constructing even more accurate functionals, whether for broadly applicable ones or ones that target good performance for particular classes of systems. At this point, it is not clear that all our identified desirable features for the enhancement factor are mutually compatible and will lead to clear improvements across all classes of van der Waals complexes. Currently ongoing work will clarify this question and seeks to develop an updated variant of the vdW-DF family that implements a maximum of these features. The optimization of such a new vdW-DF variant is not an easy task—large amounts of benchmark calculations, covering large datasets and different classes of van der Waals complexes, are needed to ensure a meaningful local minimum in the high-dimensional parameter space of not only the exchange but also the non-local correlation energy. More evidence supporting the impact of our reduced-gradient analysis on improving vdW-DF will thus be addressed and provided in our future work showcasing the utility of this insight for the development of non-local functionals. While this paper emphasizes how the effects play out for the vdW-DF family of functionals, the same analysis approach may prove fruitful when analyzing the performance of other approaches to describe van der Waals binding within DFT.

## ACKNOWLEDGEMENT

This work was supported by the U.S. National Science Foundation Grant No. DMR-1712425. The computations in this work were done on the high-performance cluster Saga and Fram managed by UNINETT Sigma2. Work in Norway was supported in part by the Research Council of Norway in the FOX project (Project No. 302362).

- [1] L. Kronik and A. Tkatchenko, Understanding molecular crystals with dispersion-inclusive density functional theory: Pairwise corrections and beyond, Acc. Chem. Res. 47, 3208 (2014).
- [2] T. Rangel, K. Berland, S. Sharifzadeh, F. Brown-Altvater, K. Lee, P. Hyldgaard, L. Kronik, and J. B. Neaton, Structural and excited-state properties of oligoacene crystals from first principles, Phys. Rev. B 93, 115206 (2016).
- [3] P. J. Diemer, J. Hayes, E. Welchman, R. Hallani, S. J. Pookpanratana, C. A. Hacker, C. A. Richter, J. E. Anthony, T. Thonhauser, and O. D. Jurchescu, The influence of isomer purity on trap states and performance of organic thin-film transistors, Adv. Electron. Mater. 3, 1600294 (2017).
- [4] R. Gomez-Bombarelli, J. Aguilera-Iparraguirre, T. D. Hirzel, D. Duvenaud, D. Maclaurin, M. A. Blood-Forsythe, H. S. Chae, M. Einzinger, D.-G. Ha, T. Wu, G. Markopoulos, S. Jeon, H. Kang, H. Miyazaki, M. Numata, S. Kim, W. Huang, S. I. Hong, M. Baldo, R. P. Adams, and A. Aspuru-Guzik, Design of efficient molecular organic light-emitting diodes by a high-throughput virtual screening and experimental approach, Nat. Mater.

- **15**, 1120 (2016).
- [5] K. Lee, B. Kolb, T. Thonhauser, D. Vanderbilt, and D. C. Langreth, Structure and energetics of a ferroelectric organic crystal of phenazine and chloranilic acid, Phys. Rev. B 86, 104102 (2012).
- [6] S. Ishibashi, S. Horiuchi, and R. Kumai, Computational findings of metastable ferroelectric phases of squaric acid, Phys. Rev. B 97, 184102 (2018).
- [7] A. M. Reilly and A. Tkatchenko, Role of dispersion interactions in the polymorphism and entropic stabilization of the aspirin crystal, Phys. Rev. Lett. 113, 055701 (2014).
- [8] K. Tan, S. Zuluaga, E. Fuentes, E. C. Mattson, J.-F. Veyan, H. Wang, J. Li, T. Thonhauser, and Y. J. Chabal, Trapping gases in metal-organic frameworks with a selective surface molecular barrier layer, Nat. Commun. 7, 13871 (2016).
- [9] H. Wang, X. Dong, J. Lin, S. J. Teat, S. Jensen, J. Cure, E. V. Alexandrov, Q. Xia, K. Tan, Q. Wang, D. H. Olson, D. M. Proserpio, Y. J. Chabal, T. Thonhauser, J. Sun, Y. Han, and J. Li, Topologically guided tuning of Zr-MOF pore structures for highly selective separation of C<sub>6</sub> alkane isomers, Nat. Commun. 9, 1745 (2018).

- [10] B. Li, X. Dong, H. Wang, D. Ma, K. Tan, S. Jensen, B. J. Deibert, J. Butler, J. Cure, Z. Shi, T. Thonhauser, Y. J. Chabal, Y. Han, and J. Li, Capture of organic iodides from nuclear waste by metal-organic frameworkbased molecular traps, Nat. Commun. 8, 485 (2017).
- [11] S. Jensen, K. Tan, W. P. Lustig, D. S. Kilin, J. Li, Y. J. Chabal, and T. Thonhauser, Structure-driven photoluminescence enhancement in a Zn-based metal-organic framework, Chem. Mater. 31, 7933 (2019).
- [12] J. Cure, E. Mattson, K. Cocq, H. Assi, S. Jensen, K. Tan, M. Catalano, S. Yuan, H. Wang, L. Feng, P. Zhang, S. Kwon, J.-F. Veyan, Y. Cabrera, G. Zhang, J. Li, M. Kim, H.-C. Zhou, Y. J. Chabal, and T. Thonhauser, High stability of ultra-small and isolated gold nanoparticles in metal-organic framework materials, J. Mater. Chem. A 7, 17536 (2019).
- [13] S. Grimme, Accurate description of van der Waals complexes by density functional theory including empirical corrections, J. Comput. Chem. 25, 1463 (2004).
- [14] S. Grimme, J. Antony, T. Schwabe, and C. Mück-Lichtenfeld, Density functional theory with dispersion corrections for supramolecular structures, aggregates, and complexes of (bio)organic molecules, Org. Biomol. Chem. 5, 741 (2007).
- [15] S. Grimme, Density functional theory with London dispersion corrections, WIREs Comput. Mol. Sci. 1, 211 (2011).
- [16] A. Tkatchenko and M. Scheffler, Accurate molecular van der Waals interactions from ground-state electron density and free-atom reference data, Phys. Rev. Lett. 102, 073005 (2009).
- [17] A. Tkatchenko, R. A. DiStasio, R. Car, and M. Scheffler, Accurate and efficient method for many-body van der Waals interactions, Phys. Rev. Lett. 108, 236402 (2012).
- [18] A. Ambrosetti, A. M. Reilly, R. A. DiStasio, and A. Tkatchenko, Long-range correlation energy calculated from coupled atomic response functions, J. Chem. Phys. 140, 18A508 (2014).
- [19] A. Ambrosetti, N. Ferri, R. A. DiStasio, and A. Tkatchenko, Wavelike charge density fluctuations and van der Waals interactions at the nanoscale, Science 351, 1171 (2016).
- [20] O. A. Vydrov and T. Van Voorhis, Nonlocal van der Waals density functional made simple, Phys. Rev. Lett. 103, 063004 (2009).
- [21] O. A. Vydrov and T. Van Voorhis, Dispersion interactions from a local polarizability model, Phys. Rev. A 81, 062708 (2010).
- [22] O. A. Vydrov and T. Van Voorhis, Nonlocal van der Waals density functional: The simpler the better, J. Chem. Phys. 133, 244103 (2010).
- [23] S. Grimme, A. Hansen, J. G. Brandenburg, and C. Bannwarth, Dispersion-corrected mean-field electronic structure methods, Chem. Rev. 116, 5105 (2016).
- [24] K. Szalewicz, Symmetry-adapted perturbation theory of intermolecular forces, WIREs Comput. Mol. Sci. 2, 254 (2012).
- [25] L. A. Burns, A. Vazquez-Mayagoitia, B. G. Sumpter, and C. D. Sherrill, Density-functional approaches to noncovalent interactions: A comparison of dispersion corrections (DFT-D), exchange-hole dipole moment (XDM) theory, and specialized functionals, J. Chem. Phys. 134, 084107 (2011).

- [26] J. Klimes and A. Michaelides, Perspective: Advances and challenges in treating van der Waals dispersion forces in density functional theory, J. Chem. Phys. 137, 120901 (2012).
- [27] M. Dion, H. Rydberg, E. Schröder, D. C. Langreth, and B. I. Lundqvist, van der Waals density functional for general geometries, Phys. Rev. Lett. 92, 246401 (2004).
- [28] T. Thonhauser, S. Zuluaga, C. A. Arter, K. Berland, E. Schröder, and P. Hyldgaard, Spin signature of nonlocal correlation binding in metal-organic frameworks, Phys. Rev. Lett. 115, 136402 (2015).
- [29] D. C. Langreth, B. I. Lundqvist, S. D. Chakarova-Käck, V. R. Cooper, M. Dion, P. Hyldgaard, A. K. Kelkkanen, J. Kleis, L. Kong, S. Li, P. G. Moses, E. D. Murray, A. Puzder, H. Rydberg, E. Schröder, and T. Thonhauser, A density functional for sparse matter, J. Phys.: Condens. Matter 21, 084203 (2009).
- [30] K. Berland, V. R. Cooper, K. Lee, E. Schröder, T. Thonhauser, P. Hyldgaard, and B. I. Lundqvist, van der Waals forces in density functional theory: A review of the vdW-DF method, Rep. Prog. Phys. 78, 066501 (2015).
- [31] P. Hyldgaard, Y. Jiao, and V. Shukla, Screening nature of the van der Waals density functional method: A review and analysis of the many-body physics foundation, J. Phys.: Condens. Matter 32, 393001 (2020).
- [32] D. Chakraborty, K. Berland, and T. Thonhauser, Nextgeneration nonlocal van der Waals density functional, J. Chem. Theory Comput. 16, 5893 (2020).
- [33] J. P. Perdew, K. Burke, and M. Ernzerhof, Generalized gradient approximation made simple, Phys. Rev. Lett. 77, 3865 (1996).
- [34] D. J. Lacks and R. G. Gordon, Pair interactions of raregas atoms as a test of exchange-energy-density functionals in regions of large density gradients, Phys. Rev. A 47, 4681 (1993).
- [35] Y. Zhang, W. Pan, and W. Yang, Describing van der Waals interaction in diatomic molecules with generalized gradient approximations: The role of the exchange functional, J. Chem. Phys. 107, 7921 (1997).
- [36] F. O. Kannemann and A. D. Becke, van der Waals interactions in density-functional theory: Rare-gas diatomics, J. Chem. Theory Comput. 5, 719 (2009).
- [37] E. D. Murray, K. Lee, and D. C. Langreth, Investigation of exchange energy density functional accuracy for interacting molecules, J. Chem. Theory Comput. 5, 2754 (2009).
- [38] R. Laplaza, F. Peccati, R. A. Boto, C. Quan, A. Carbone, J.-P. Piquemal, Y. Maday, and J. Contreras-García, NCI-PLOT and the analysis of noncovalent interactions using the reduced density gradient, WIREs Comput. Mol. Sci. 11, e1497 (2021).
- [39] E. R. Johnson, S. Keinan, P. Mori-Sánchez, J. Contreras-García, A. J. Cohen, and W. Yang, Revealing Noncovalent Interactions, J. Am. Chem. Soc. 132, 6498 (2010).
- [40] H. Rydberg, Nonlocal Correlations in Density Functional Theory, Ph.D. thesis, Chalmers University of Technology and Göteborg University (2001).
- [41] K. Berland, Connected by Voids: Interactions and Screening in Sparse Matter, Ph.D. thesis, Chalmers University of Technology (2012).
- [42] P. Hyldgaard, K. Berland, and E. Schröder, Interpretation of van der Waals density functionals, Phys. Rev. B 90, 075148 (2014).

- [43] E. Schröder, V. R. Cooper, K. Berland, B. I. Lundqvist, P. Hyldgaard, and T. Thonhauser, The vdW-DF family of nonlocal exchange-correlation functionals, in Non-Covalent Interactions in Quantum Chemistry and Physics, Theory Applications, edited by A. O. de la Roza and G. A. DiLabio (Elsevier, Amsterdam, 2017) Chap. 8, pp. 241–274.
- [44] J. P. Perdew, M. Ernzerhof, and K. Burke, Rationale for mixing exact exchange with density functional approximations, The Journal of Chemical Physics 105, 9982 (1996).
- [45] P. J. Stephens, F. J. Devlin, C. F. Chabalowski, and M. J. Frisch, Ab initio calculation of vibrational absorption and circular dichroism spectra using density functional force fields, J. Phys. Chem. 98, 11623 (1994).
- [46] S. Grimme, J. Antony, S. Ehrlich, and H. Krieg, A consistent and accurate ab initio parametrization of density functional dispersion correction (dft-d) for the 94 elements h-pu, J. Chem. Phys. 132, 154104 (2010).
- [47] J. P. Perdew, K. Burke, and Y. Wang, Generalized gradient approximation for the exchange-correlation hole of a many-electron system, Phys. Rev. B 54, 16533 (1996).
- [48] Y. Zhang and W. Yang, Comment on "Generalized gradient approximation made simple", Phys. Rev. Lett. 80, 890 (1998).
- [49] I. Hamada and M. Otani, Comparative van der Waals density-functional study of graphene on metal surfaces, Phys. Rev. B 82, 153412 (2010).
- [50] H. Yildirim, T. Greber, and A. Kara, Trends in adsorption characteristics of benzene on transition metal surfaces: Role of surface chemistry and van der Waals interactions, J. Phys. Chem. C 117, 20572 (2013).
- [51] W. Liu, J. Carrasco, B. Santra, A. Michaelides, M. Scheffler, and A. Tkatchenko, Benzene adsorbed on metals: Concerted effect of covalency and van der Waals bonding, Phys. Rev. B 86, 245405 (2012).
- [52] K. Berland, C. A. Arter, V. R. Cooper, K. Lee, B. I. Lundqvist, E. Schröder, T. Thonhauser, and P. Hyldgaard, van der Waals density functionals built upon the electron-gas tradition: Facing the challenge of competing interactions, J. Chem. Phys. 140, 18A539 (2014).
- [53] K. Lee, E. D. Murray, L. Kong, B. I. Lundqvist, and D. C. Langreth, Higher-accuracy van der Waals density functional, Phys. Rev. B 82, 081101(R) (2010).
- [54] V. R. Cooper, van der Waals density functional: An appropriate exchange functional, Phys. Rev. B 81, 161104(R) (2010).
- [55] This expressions will give energies in "a.u.", i.e. Hartree.
- [56] R. M. Martin, Electronic Structure: Basic Theory and Practical Methods (Cambridge University Press, 2004).
- [57] L. C. Balbás, J. L. Martins, and J. M. Soler, Evaluation of exchange-correlation energy, potential, and stress, Phys. Rev. B 64, 165110 (2001).
- [58] P. Giannozzi, O. Andreussi, T. Brumme, O. Bunau, M. Buongiorno Nardelli, M. Calandra, R. Car, C. Cavazzoni, D. Ceresoli, M. Cococcioni, N. Colonna, I. Carnimeo, A. Dal Corso, S. de Gironcoli, P. Delugas, R. A. DiStasio, A. Ferretti, A. Floris, G. Fratesi, G. Fugallo, R. Gebauer, U. Gerstmann, F. Giustino, T. Gorni, J. Jia, M. Kawamura, H.-Y. Ko, A. Kokalj, E. Küçükbenli, M. Lazzeri, M. Marsili, N. Marzari, F. Mauri, N. L. Nguyen, H.-V. Nguyen, A. Otero-de-la Roza, L. Paulatto,

- S. Poncé, D. Rocca, R. Sabatini, B. Santra, M. Schlipf, A. P. Seitsonen, A. Smogunov, I. Timrov, T. Thonhauser, P. Umari, N. Vast, X. Wu, and S. Baroni, Advanced capabilities for materials modelling with Quantum ESPRESSO, J. Phys.: Condens. Matter 29, 465901 (2017).
- [59] K. F. Garrity, J. W. Bennett, K. M. Rabe, and D. Vanderbilt, Pseudopotentials for high-throughput DFT calculations, Comput. Mater. Sci. 81, 446 (2014).
- [60] H. Peng, Z.-H. Yang, J. P. Perdew, and J. Sun, Versatile van der Waals density functional based on a metageneralized gradient approximation, Phys. Rev. X 6, 041005 (2016).
- [61] T. Björkman, A. Gulans, A. V. Krasheninnikov, and R. M. Nieminen, van der Waals bonding in layered compounds from advanced density-functional first-principles calculations, Phys. Rev. Lett. 108, 235502 (2012).
- [62] T. Björkman, Testing several recent van der Waals density functionals for layered structures, J. Chem. Phys. 141, 074708 (2014).
- [63] A. M. Reilly and A. Tkatchenko, Understanding the role of vibrations, exact exchange, and many-body van der Waals interactions in the cohesive properties of molecular crystals, J. Chem. Phys. 139, 024705 (2013).
- [64] K. Berland, T. L. Einstein, and P. Hyldgaard, Rings sliding on a honeycomb network: Adsorption contours, interactions, and assembly of benzene on Cu (111), Phys. Rev. B 80, 155431 (2009).
- [65] L. Gráfová, M. Pitoňák, J. Řezáč, and P. Hobza, Comparative study of selected wave function and density functional methods for noncovalent interaction energy calculations using the extended S22 data set, J. Chem. Theory Comput. 6, 2365 (2010).
- [66] J. Klimeš, D. R. Bowler, and A. Michaelides, Chemical accuracy for the van der Waals density functional, J. Phys.: Condens. Matter 22, 022201 (2010).
- [67] K. Berland and P. Hyldgaard, Exchange functional that tests the robustness of the plasmon description of the van der Waals density functional, Phys. Rev. B 89, 035412 (2014).
- [68] I. Hamada, van der Waals density functional made accurate, Phys. Rev. B 89, 121103(R) (2014).
- [69] J. P. Perdew and Y. Wang, Accurate and simple density functional for the electronic exchange energy: Generalized gradient approximation, Phys. Rev. B 33, 8800 (1986).
- [70] P. Jurecka, J. Sponer, J. Cerny, and P. Hobza, Benchmark database of accurate (MP2 and CCSD(T) complete basis set limit) interaction energies of small model complexes, DNA base pairs, and amino acid pairs, Phys. Chem. Chem. Phys. 8, 1985 (2006).
- [71] K. Berland and P. Hyldgaard, Analysis of van der Waals density functional components: Binding and corrugation of benzene and  $C_{60}$  on boron nitride and graphene, Phys. Rev. B 87, 205421 (2013).
- [72] F. Tran, L. Kalantari, B. Traoré, X. Rocquefelte, and P. Blaha, Nonlocal van der Waals functionals for solids: Choosing an appropriate one, Phys. Rev. Mater. 3, 063602 (2019).
- [73] T. Bjorkman, A. Gulans, A. V. Krasheninnikov, and R. M. Nieminen, Are we van der Waals ready?, J. Phys.: Condens. Matter 24, 424218 (2012).
- [74] J. Moellmann and S. Grimme, DFT-D3 study of some molecular crystals, J. Phys. Chem. C 118, 7615 (2014).

# — Supplementary Information —

# Reduced-gradient analysis of van der Waals complexes

T. Jenkins,  $^{1,2}$  K. Berland,  $^{3,*}$  and T. Thonhauser  $^{1,2,\dagger}$ 

<sup>1</sup>Department of Physics, Wake Forest University, Winston-Salem, NC 27109, USA.
<sup>2</sup>Center for Functional Materials, Wake Forest University, Winston-Salem, NC 27109, USA.
<sup>3</sup>Faculty of Science and Technology, Norwegian University of Life Sciences, Norway.

(Dated: October 13, 2021)

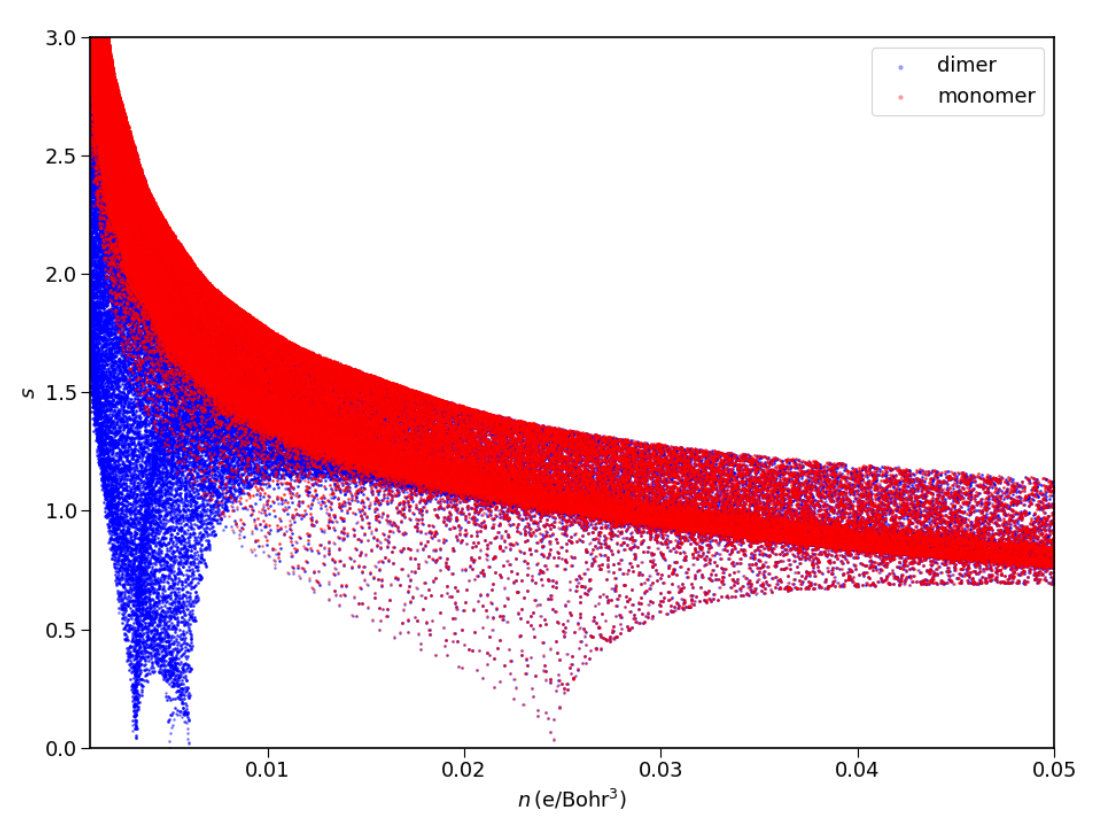


FIG. S1. Reduced-gradient s vs. charge density n scatter plot for the benzene dimer. To the left, the plot clearly shows points of s and n that are unique to the dimer and can be associated with the disk in Fig. 2 in the main manuscript. In this low-density region, we see that for s>1 the monomers start to enter, corresponding to the merger process discussed. Further to the right, we see that the monomers and dimer essentially share all the same s and n values, which corresponds to regions closer to the monomers.

 $<sup>^*</sup>$  E-mail: kristian.berland@nmbu.no

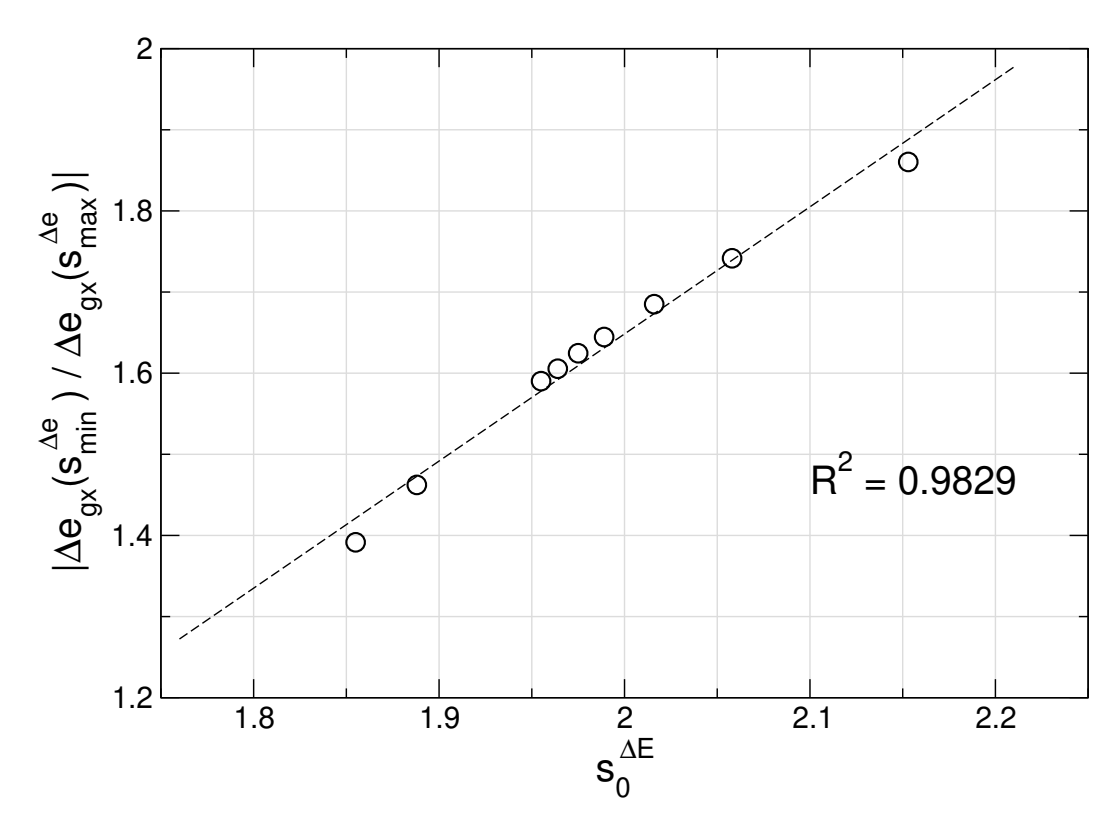


FIG. S2. Further analysis of the data shown in Fig. 4 in the main manuscript. In particular, we show here the crossover point  $s_0^{\Delta E}$ , i.e. where  $\Delta E_{\rm gx}(s)$  crosses 0, plotted with respect to the ratio of  $\Delta e_{\rm gx}$  at the extrema  $s_{\rm min}^{\Delta e}$  and  $s_{\rm max}^{\Delta e}$ . Each of the nine points corresponds to a unique exchange functional. An analysis of the shape of the curves in Fig. 4 gives a rough and simple heuristic relation between these quantities and  $F_{\rm x}(s)$  as  $s_0^{\Delta E} \approx A \cdot F_{\rm x}(s_{\rm min}^{\Delta e})/F_{\rm x}(s_{\rm max}^{\Delta e}) + B$ , where A and B are system-dependent but not functional-dependent constants. As  $\Delta e_{\rm gx}(s)$  is integrated with respect to s to give  $\Delta E_{\rm gx}(s)$ , the net contributions from the negative and positive peaks cancel out around  $s_0^{\Delta E} \approx 2$ . Since then the net positive contributions stem from s-regions beyond that crossing point,  $\Delta E_{\rm gx}(\infty)$  is related to the position of the crossover point and the magnitude of  $F_{\rm x}(s)$  beyond it. Since this crossover is due to the cancellation of the downward and upward peaks in  $\Delta e_{\rm gx}(s)$ , it follows that its location is a function of the peaks' relative magnitudes at  $s_{\rm min}^{\Delta e}$  and  $s_{\rm max}^{\Delta e}$ , shown in this figure. If we assume that the downward and upward peaks retain overall similar shapes, we obtain the above relationship.

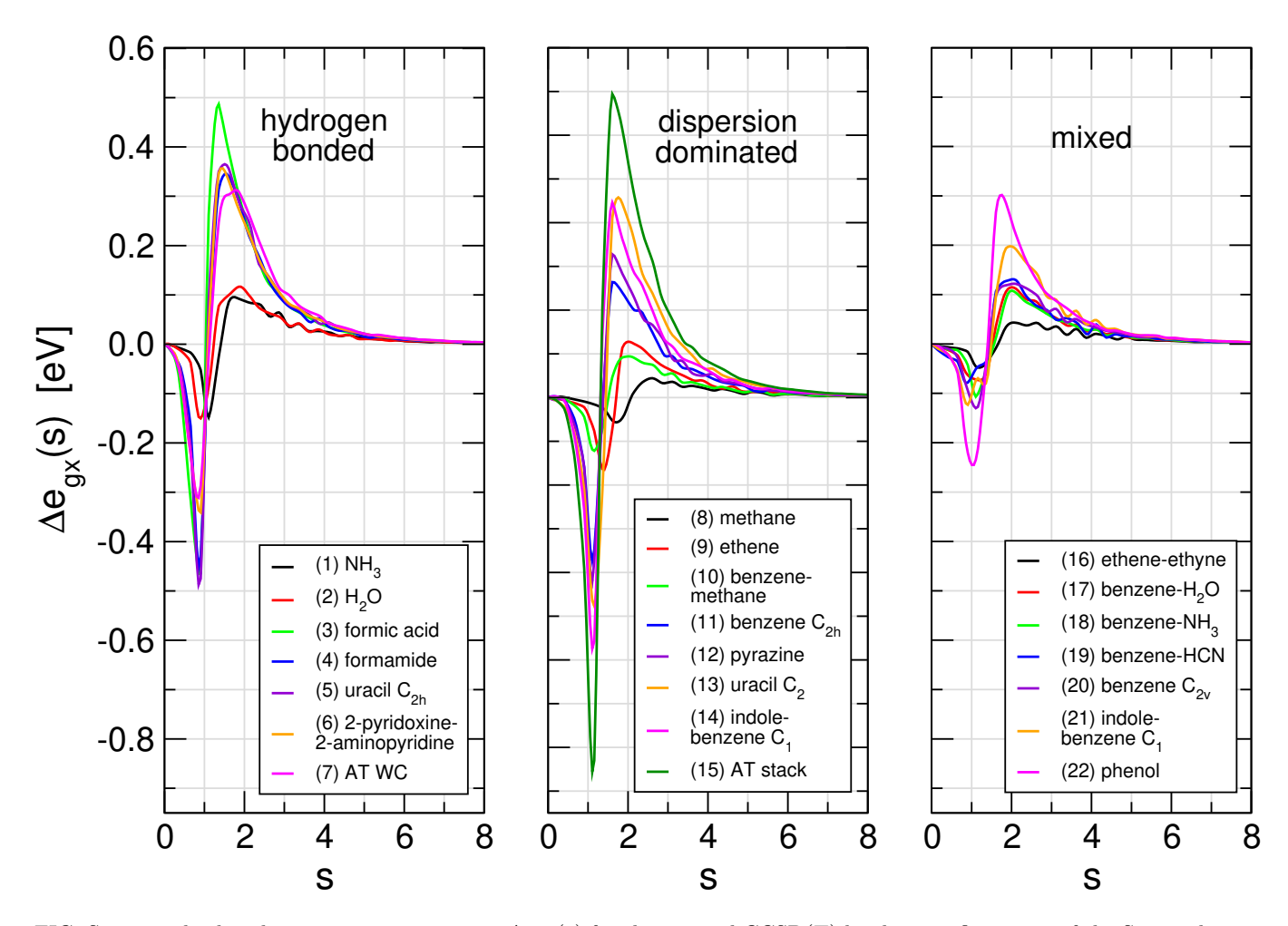


FIG. S3. s-resolved exchange interaction energy  $\Delta e_{\rm gx}(s)$  for the optimal CCSD(T) binding configuration of the S22×5 dataset of molecular dimers. Results are separated into hydrogen-bonded, dispersion-dominated, and mixed dimers of this set.

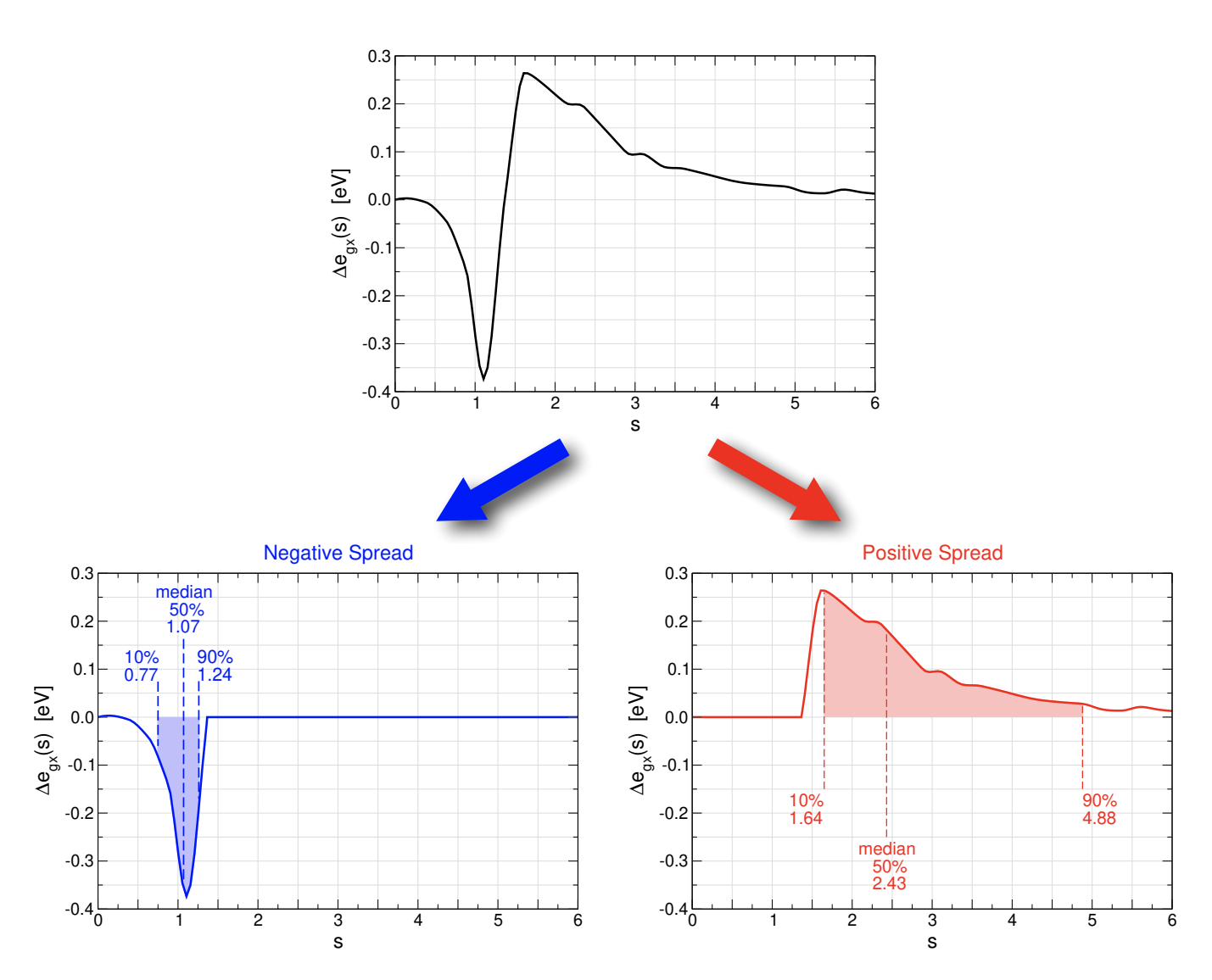


FIG. S4. Definition of the spread for the case of the benzine dimer. The  $\Delta e_{\rm gx}(s)$  curve is separated into positive and negative contributions and the spread is then evaluated separately for each of them. We define each spread as reaching from the  $10^{\rm th}$  percentile to the  $90^{\rm th}$  percentile, i.e. 40 percentiles below and above the median (which is located at the  $50^{\rm th}$  percentile). The shaded areas in these two plots correspond to the values shown in Fig. 5 in the main manuscript.

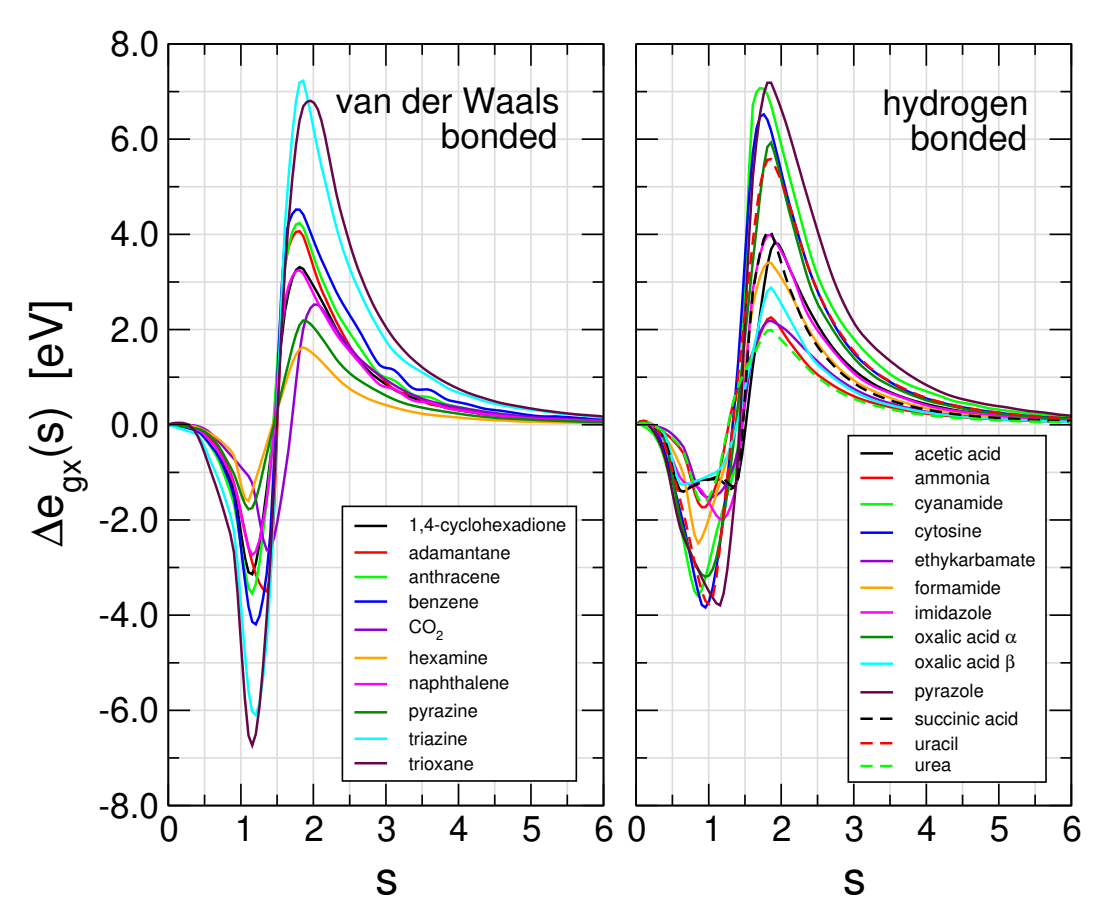


FIG. S5. s-resolved exchange interaction energy  $\Delta e_{\rm gx}(s)$  for the X23 dataset of molecular crystals. Results are separated into van der Waals-bonded and hydrogen-bonded systems.

TABLE S1. Optimized binding distances  $[\mathring{A}]$  for the S22 set of molecular dimers [1], along with the mean deviation (MD), the mean absolute deviation (MAD), and mean absolute relative deviation (MARD). CCSD(T) reference data taken from Ref. [1]. Reproduced with permission from the SI of Ref. [2]. © 2020, American Chemical Society.

System	CCSD(T)	DF1	DF2	DF1-optb88	DF1-cx	DF2-B86R	DF3-opt1	DF3-opt2
Hydrogen-bonding systems (7)								
Ammonia dimer $(C_{2h})$	3.209	3.409	3.309	3.259	3.309	3.259	3.159	3.209
Water dimer $(C_s)$	2.909	3.034	2.984	2.934	2.934	2.909	2.859	2.884
Formicacid dimer $(C_{2h})$	2.993	3.067	3.067	2.992	2.992	2.992	2.967	2.992
Formamide dimer $(C_{2h})$	3.229	3.329	3.304	3.229	3.229	3.229	3.179	3.229
Uracil dimer $(C_{2h})$	6.075	6.150	6.150	6.075	6.050	6.075	6.025	6.050
2-pyridoxine 2-aminopyridine $(C_1)$	5.136	5.211	5.211	5.111	5.111	5.111	5.086	5.111
Adenine thymine WC complex $(C_1)$	5.974	6.049	6.024	5.949	5.949	5.949	5.924	5.949
MD [Å]		0.104	0.075	0.004	0.007	0.000	-0.046	-0.014
MAD [Å]	_	0.104	0.075	0.018	0.029	0.015	0.046	0.014
MARD [%]	_	2.87	2.01	0.48	0.76	0.36	1.18	0.31
Dispersion-based systems (8)								
Methane dimer $(D_{3d})$	3.718	3.893	3.693	3.818	3.968	3.818	3.718	3.693
Ethene dimer $(D_{2d})$	3.718	4.068	3.868	3.868	4.168	3.893	3.718	3.768
Benzene methane $(C_3)$	3.716	4.066	3.891	3.841	4.016	3.866	3.741	3.791
Benzene dimer $(C_{2h})$	3.765	4.214	4.064	3.939	4.089	3.989	3.864	3.914
Pyrazine dimer $(C_s)$	3.479	3.854	3.729	3.604	3.704	3.654	3.529	3.579
Uracil dimer $(C_2)$	3.166	3.391	3.291	3.191	3.241	3.216	3.116	3.166
Indole benzene $(C_1)$	3.498	3.898	3.798	3.648	3.748	3.698	3.573	3.623
Adenine thymine $(C_1)$	3.172	3.471	3.371	3.246	3.271	3.246	3.171	3.196
MD [Å]	_	0.328	0.184	0.116	0.247	0.144	0.025	0.062
MAD [Å]	_	0.328	0.191	0.116	0.247	0.144	0.038	0.069
MARD [%]		9.28	5.42	3.22	6.83	4.01	1.06	1.91
Others (7)								
Ethene ethyne $(C_{2v})$	4.422	4.572	4.472	4.422	4.522	4.447	4.322	4.372
Benzene water $(C_s)$	3.380	3.581	3.481	3.381	3.431	3.381	3.281	3.331
Benzene ammonia $(C_s)$	3.560	3.835	3.685	3.610	3.735	3.635	3.510	3.560
Benzene HCN $(C_s)$	3.950	4.200	4.100	4.000	4.025	4.000	3.900	3.950
Benzene dimer $(C_{2v})$	4.909	5.234	5.134	5.034	5.109	5.059	4.934	4.984
Indole benzene $(C_1)$	4.884	5.159	5.084	4.984	5.034	4.984	4.909	4.934
Phenol dimer $(C_1)$	4.921	5.120	5.020	4.945	4.970	4.945	4.870	4.920
MD [Å]	_	0.239	0.136	0.050	0.114	0.061	-0.043	0.004
MAD [Å]	_	0.239	0.136	0.050	0.114	0.061	0.057	0.032
MARD [%]		5.67	3.16	1.11	2.68	1.37	1.42	0.74
Total (22)								
MD [Å]		0.228	0.134	0.059	0.128	0.072	-0.019	0.019
MAD [Å]	_	0.228	0.136	0.064	0.135	0.076	0.047	0.040
MARD [%]	_	6.09	3.62	1.68	3.58	2.01	1.21	1.03

TABLE S2. Optimized binding energy [meV] for the S22 set of molecular dimers [1], along with the mean deviation (MD), the mean absolute deviation (MAD), and mean absolute relative deviation (MARD). CCSD(T) reference data taken from Ref. [3]. Reproduced with permission from the SI of Ref. [2]. © 2020, American Chemical Society.

System	CCSD(T)	DF1	DF2	DF1-optb88	DF1-cx	DF2-B86R	DF3-opt1	DF3-opt2
Hydrogen-bonding systems (7)								
Ammonia dimer $(C_{2h})$	-135.9	-114.3	-130.8	-123.2	-114.8	-125.5	-141.8	-141.9
Water dimer $(C_s)$	-216.3	-178.4	-208.5	-203.9	-191.7	-208.1	-232.4	-226.7
Formicacid dimer $(C_{2h})$	-813.2		-737.1	-813.6	-792.8	-804.3	-899.5	-849.0
Formamide dimer $(C_{2h})$	-696.5	-569.0	-628.6	-670.3	-640.7	-659.0	-732.4	-698.7
Uracil dimer $(C_{2h})$	-895.1		-806.2	-863.5	-836.3	-846.0	-922.1	-887.8
2-pyridoxine 2-aminopyridine $(C_1)$	-734.3	-626.5	-668.9	-740.6	-723.7	-722.2	-798.2	-763.4
Adenine thymine WC complex $(C_1)$	-722.4	-598.4	-643.3	-711.6	-685.6	-689.1	-765.1	-732.6
MD [meV]		101.1	55.8	12.4	32.6	22.8	-39.7	-12.4
MAD [meV]	_	101.1	55.8	14.3	32.6	22.8	39.7	14.4
MARD [%]	_	16.78	8.03	3.53	7.22	4.24	6.46	2.87
Dispersion-based systems (8)								
Methane dimer $(D_{3d})$	-22.9	-37.0	-30.8	-24.3	-31.8	-20.6	-20.4	-28.1
Ethene dimer $(D_{2d})$	-63.8	-64.9	-64.2	-57.1	-57.8	-49.7	-59.4	-65.7
Benzene methane $(C_3)$	-62.8	-67.4	-63.4	-66.9	-62.6	-53.5	-63.0	-66.7
Benzene dimer $(C_{2h})$	-115.1	-135.7	-124.8	-150.4	-129.2	-106.8	-122.4	-129.4
Pyrazine dimer $(C_s)$	-184.5	-182.7	-175.9	-206.0	-179.7	-161.6	-183.4	-188.9
Uracil dimer $(C_2)$	-425.2	-395.0	-392.7	-452.8	-404.3	-383.4	-424.2	-428.6
Indole benzene $(C_1)$	-196.2	-205.1	-198.4	-239.2	-202.4	-180.6	-203.6	-213.3
Adenine thymine $(C_1)$	-508.7	-454.1	-458.2	-540.5	-474.2	-453.4	-504.2	-511.2
MD [meV]	_	4.7	8.8	-19.8	4.6	21.2	-0.2	-6.6
MAD [meV]	_	17.0	14.0	21.4	12.0	21.2	3.5	6.6
MARD [%]	_	14.03	8.49	12.53	9.84	11.91	3.71	7.14
Others (7)								
Ethene ethyne $(C_{2v})$	-64.9	-68.3	-68.3	-67.3	-65.7	-62.5	-70.3	-72.3
Benzene water $(C_s)$	-142.0	-121.2	-125.4	-135.9	-125.9	-124.3	-145.4	-142.6
Benzene ammonia $(C_s)$	-100.3	-93.0	-91.8	-98.0	-91.6	-85.5	-99.2	-100.9
Benzene HCN $(C_s)$	-196.9	-162.0	-163.7	-183.9	-175.0	-171.6	-196.8	-192.3
Benzene dimer $(C_{2v})$	-117.8	-113.7	-105.4	-122.6	-113.6	-97.4	-112.5	-114.7
Indole benzene $(C_1)$	-244.0	-212.0	-202.5	-238.6	-225.9	-206.5	-233.0	-231.0
Phenol dimer $(C_1)$	-307.8	-248.9	-269.8	-295.2	-262.1	-263.5	-305.0	-294.8
MD [meV]	_	22.1	21.0	4.6	16.3	23.2	1.7	3.6
MAD [meV]	_	23.0	22.0	6.6	16.5	23.2	4.2	6.0
MARD [%]		11.50	11.75	3.88	8.31	12.97	3.11	3.85
Total								
MD [meV]		40.9	27.6	-1.8	17.2	22.3	-12.2	-5.2
MAD [meV]		45.7	29.8	-1.8 14.5	20.0	22.3	-12.2 $15.2$	-3.2 8.9
MARD [%]		14.10	9.38	6.91	8.52	9.81	4.39	4.74
1111111 [/0]		14.10	9.00	0.91	0.02	9.01	4.09	4.14

TABLE S3. Binding energies [meV] for the S22×5 set of molecular dimers at the "1.0" separation [4], along with the mean deviation (MD), the mean absolute deviation (MAD), and mean absolute relative deviation (MARD). CCSD(T) reference data taken from Ref. [4]. Reproduced with permission from the SI of Ref. [2]. © 2020, American Chemical Society.

	1				<u> </u>		v	
System	CCSD(T)	DF1	DF2	DF1-optB88	DF1-cx	DF2-B86R	DF3-opt1	DF3-opt2
H-bond-dominated (7)								
Ammonia dimer $(C_{2h})$	126.2	-105.3	-129.1	-123.1	-113.3	-125.6	-140.8	-141.7
Water dimer $(C_s)$		-105.3 $-172.7$	-129.1 $-207.4$	-125.1 $-205.0$	-113.3 $-192.7$	-125.0 $-209.2$	-140.8 $-231.3$	-141.7 $-226.9$
Formicacid dimer $(C_{2h})$	-806.1	-661.3	-207.4 $-725.8$	-205.0 $-816.6$	-795.7	-203.2 $-807.2$	-291.3 $-899.2$	-220.9 $-851.1$
Formamide dimer $(C_{2h})$	-691.7	-555.0	-618.9	-670.8	-641.2	-659.4	-727.6	-696.3
Uracil dimer $(C_{2h})$	-887.2	-743.3	-803.0	-868.0	-840.1	-850.5	-921.2	-891.1
2-pyridoxine 2-aminopyridine $(C_1)$	-724.2	-622.1	-665.2	-744.0	-726.1	-725.5	-794.7	-764.2
Adenine thymine WC complex $(C_1)$	-709.9	-591.8	-638.8	-711.7	-685.2	-689.2	-759.4	-732.1
MD [meV]		102.8	54.7	4.5	25.2	14.9	-43.3	-18.9
MAD [meV]	_	102.8	54.7	13.7	25.7	15.6	43.3	18.9
MARD [%]	_	18.18	8.16	3.42	6.43	3.25	6.85	3.53
WITHED [70]		10.10	0.10	0.12	0.10	0.20	0.00	0.00
Dispersion-dominated (8)								
Methane dimer $(D_{3d})$	-23.0	-35.1	-30.8	-23.7	-27.7	-20.0	-20.4	-28.1
Ethene dimer $(D_{2d})$	-64.2	-47.9	-60.8	-54.7	-41.6	-46.5	-59.3	-65.2
Benzene methane $(C_3)$	-65.0	-52.9	-58.1	-65.1	-55.8	-50.6	-62.8	-66.1
Benzene dimer $(C_{2h})$	-121.9	-88.1	-96.8	-141.6	-112.0	-93.7	-119.1	-123.4
Pyrazine dimer $(C_s)$	-195.6	-134.6	-148.5	-198.3	-165.6	-151.1	-181.3	-184.7
Uracil dimer $(C_2)$	-428.0	-364.0	-382.1	-453.9	-402.7	-384.0	-419.0	-425.5
Indole benzene $(C_1)$	-224.6	-134.0	-155.1	-227.2	-184.3	-164.9	-199.8	-205.9
Adenine thymine $(C_1)$	-529.9	-381.1	-420.8	-536.1	-466.9	-447.8	-502.4	-508.7
MD [meV]	_	51.8	37.4	-6.0	24.4	36.7	11.0	5.6
MAD [meV]	_	54.9	39.3	8.4	25.6	36.7	11.0	7.7
MARD [%]	_	29.88	19.57	5.50	16.13	20.14	6.31	5.63
Others (7)								
Ethene ethyne $(C_{2v})$	-64.6	-65.6	-68.0	-67.2	-64.7	-62.3	-69.4	-72.1
Benzene water $(C_s)$	-141.8	-113.6	-123.4	-135.9	-125.5	-124.4	-142.6	-142.0
Benzene ammonia $(C_s)$	-101.9	-82.8	-88.7	-97.5	-88.6	-84.7	-98.4	-100.8
Benzene HCN $(C_s)$	-196.0	-147.9	-157.1	-183.8	-174.3	-171.5	-195.9	-192.4
Benzene dimer $(C_{2v})$	-121.4	-91.6	-94.1	-119.5	-107.3	-93.0	-112.0	-113.4
Indole benzene $(C_1)$	-248.9	-184.6	-186.4	-235.5	-219.9	-202.5	-232.6	-229.9
Phenol dimer $(C_1)$	-305.7	-232.0	-264.0	-295.3	-261.4	-263.4	-303.2	-294.9
MD [meV]	_	37.5	28.4	6.5	19.8	25.5	3.8	5.0
MAD [meV]	_	37.7	29.3	7.2	19.8	25.5	5.4	7.2
MARD [%]		19.88	16.03	4.14	10.52	14.43	3.80	4.64
Total (22)								
MD [meV]	_	63.5	40.0	1.3	23.2	26.2	-8.6	-2.4
MAD [meV]	_	64.7	41.0	9.7	23.8	26.4	19.5	11.1
MARD [%]	_	22.97	14.81	4.41	11.26	12.95	5.68	4.64

TABLE S4. Layer separation [Å] and layer binding energies  $[meV/Å^2]$  for nine layered systems. Reference data for the separation is taken from experiment and for the binding energy from RPA, as detailed in Ref. [5, 6] and references therein. Reproduced with permission from Ref. [2]. © 2020, American Chemical Society.

G .	c	DE1	DEO	DE1 / D00	DE1	DE0 D0CD	DE9 /1	DE9 49
System	ref.	DF1	DF2	DF1-optB88	DF1-cx	DF2-B86R	DF3-opt1	DF3-opt2
Layer separation								
BN	3.35	3.54	3.47	3.28	3.21	3.26	3.24	3.23
graphite	3.35	3.55	3.49	3.34	3.28	3.31	3.31	3.29
$HfS_2$	5.84	5.95	6.00	5.82	5.75	5.78	5.74	5.77
$HfSe_2$	6.16	6.46	6.53	6.30	6.23	6.27	6.22	6.26
$HfTe_2$	6.65	7.25	7.27	6.78	6.55	6.67	6.59	6.63
$MoS_2$	6.15	6.62	6.57	6.26	6.12	6.18	6.14	6.15
$MoSe_2$	6.46	7.03	7.02	6.62	6.45	6.54	6.48	6.51
$PdTe_2$	5.11	5.65	6.02	5.36	5.14	5.25	5.19	5.23
$WS_2$	6.16	6.58	6.53	6.28	6.15	6.21	6.17	6.18
MD [Å]	_	0.58	0.59	0.12	-0.07	0.03	-0.03	-0.01
MAD [Å]	_	0.58	0.59	0.16	0.09	0.10	0.08	0.09
MARD [%]	_	6.81	7.26	1.96	1.30	1.31	1.13	1.29
Layer binding ene	rgy							
BN	14.4	19.02	18.30	25.33	23.80	21.17	20.17	22.04
graphite	18.3	20.54	20.21	27.00	25.27	23.28	21.01	23.95
$HfS_2$	16.1	15.08	16.33	21.51	20.20	19.16	17.90	20.25
$HfSe_2$	17.0	15.68	16.22	21.38	20.48	19.08	18.08	19.94
$HfTe_2$	18.6	15.72	16.04	22.71	24.55	21.97	21.37	23.04
$MoS_2$	20.5	18.76	19.61	25.73	24.36	23.28	21.41	24.14
$MoSe_2$	19.6	17.52	18.10	24.73	24.37	22.34	21.11	23.04
$PdTe_2$	40.1	23.59	21.73	42.86	51.60	44.33	46.73	45.95
$WS_2$	20.2	18.07	18.84	25.83	24.23	23.17	21.42	23.97
$\overline{\mathrm{MD}\ [\mathrm{meV/\AA^2}]}$		-2.31	-2.16	5.81	5.43	3.67	2.71	4.61
$\mathrm{MAD} \; [\mathrm{meV/\mathring{A}^2}]$	_	3.84	3.50	5.81	5.43	3.67	2.71	4.61
MARD [%]	_	16.08	13.53	32.36	26.31	19.60	13.55	24.38

TABLE S5. Adsorption distance [Å], adsorption energy [eV], and their relative deviation (RD) for benzene adsorbed on the Cu, Ag, and Au (111) surface. Reference data is available in Refs. [7–11]. Reproduced with permission from Ref. [2]. © 2020, American Chemical Society.

System	expt.	DF1	DF2	DF1-optB88	DF1-cx	DF2-B86R	DF3-opt1	DF3-opt2
Cu(111)/benz	sene							
distance [Å]	2.83	3.60	3.49	3.34	2.95	3.10	2.87	3.01
RD [%]		27.92	24.05	18.62	4.51	10.13	1.86	7.04
energy [eV]	$0.68 {\pm} 0.04$	0.464	0.430	0.595	0.708	0.530	0.646	0.617
RD [%]	_	-31.74	-36.82	-12.52	4.06	-22.04	-4.95	-9.20
Ag(111)/benz	ene							
distance [Å]	2.97	3.58	3.45	3.33	3.05	3.14	2.99	3.07
RD [%]		20.44	16.05	12.24	2.64	5.61	0.54	3.28
energy [eV]	$0.63 {\pm} 0.05$	0.513	0.478	0.673	0.669	0.608	0.655	0.668
RD [%]		-18.63	-24.10	6.82	6.20	-3.47	4.02	5.99
Au(111)/benz	xene							
distance [Å]	3.05	3.50	3.36	3.28	3.06	3.12	3.01	3.06
RD [%]	_	14.81	10.15	7.55	0.20	2.18	1.47	0.28
energy [eV]	$0.71 \pm 0.03$	0.601	0.575	0.771	0.767	0.653	0.724	0.712
RD [%]		-15.39	-18.97	8.57	7.97	-8.00	1.96	0.21

TABLE S6. Mean deviation (MD), mean absolute deviation (MAD), and mean absolute relative deviation (MARD) for the cohesive energy per monomer [eV] and the third-root volume  $[\mathring{A}]$  for the X23 set of molecular dimers [12]. Reference data taken from the same reference. Reproduced with permission from Ref. [2]. © 2020, American Chemical Society.

System	DF1	DF2	DF1-optb88	DF1-cx	DF2-B86R	DF3-opt1	DF3-opt2
Cohesive ene							
vdW-bonded sy	` /						
MD [eV]	-0.083	-0.051	-0.228	-0.074	0.002	-0.097	-0.088
MAD [eV]	0.083	0.065	0.228	0.074	0.036	0.097	0.088
MARD [%]	12.81	9.84	31.62	10.43	4.46	13.84	12.51
$Hydrogen ext{-}bond$	led systems (1	3)					
MD [eV]	0.002	-0.019	-0.195	-0.082	-0.035	-0.177	-0.127
MAD [eV]	0.042	0.048	0.195	0.088	0.052	0.177	0.127
$\mathrm{MARD}~[\%]$	3.74	4.73	20.51	9.33	5.32	19.34	13.99
Average over o	ıll systems (25	3)					
MD [eV]	-0.035	-0.033	-0.209	-0.079	-0.019	-0.142	-0.110
MAD [eV]	0.060	0.055	0.209	0.082	0.045	0.142	0.110
MARD [%]	7.68	6.95	25.34	9.81	4.95	16.95	13.34
$\sqrt[3]{V}$							
vdW-bonded sy	stems (10)						
MD [Å]	0.176	0.019	-0.105	0.035	-0.072	-0.169	-0.132
MAD [Å]	0.176	0.048	0.105	0.051	0.072	0.169	0.132
MARD [%]	2.54	0.69	1.47	0.77	0.99	2.37	1.85
Hydrogen-bond	led systems (1	3)					
MD [Å]	0.176	0.045	-0.106	-0.010	-0.075	-0.175	-0.128
MAD [Å]	0.176	0.053	0.106	0.042	0.075	0.175	0.128
MARD [%]	2.60	0.75	1.65	0.64	1.18	2.70	1.98
Average over o	ull systems (25	3)					
MD [Å]	0.176	0.034	-0.106	0.010	-0.074	-0.172	-0.130
MAD [Å]	0.176	0.051	0.106	0.046	0.074	0.172	0.130
MARD [%]	2.57	0.72	1.57	0.70	1.10	2.56	1.92

- P. Jurecka, J. Sponer, J. Cerny, and P. Hobza, Benchmark database of accurate (MP2 and CCSD(T) complete basis set limit) interaction energies of small model complexes, DNA base pairs, and amino acid pairs, Phys. Chem. Chem. Phys. 8, 1985 (2006).
- [2] D. Chakraborty, K. Berland, and T. Thonhauser, Nextgeneration nonlocal van der Waals density functional, J. Chem. Theory Comput. 16, 5893 (2020).
- [3] M. S. Marshall, L. A. Burns, and C. D. Sherrill, Basis set convergence of the coupled-cluster correction,  $\delta_{\text{MP2}}^{\text{CCSD(T)}}$ : Best practices for benchmarking non-covalent interactions and the attendant revision of the S22, NBC10, HBC6, and HSG databases, J. Chem. Phys. **135**, 194102 (2011).
- [4] L. Gráfová, M. Pitoňák, J. Řezáč, and P. Hobza, Comparative study of selected wave function and density functional methods for noncovalent interaction energy calculations using the extended S22 data set, J. Chem. Theory Comput. 6, 2365 (2010).
- [5] T. Björkman, A. Gulans, A. V. Krasheninnikov, and R. M. Nieminen, van der Waals bonding in layered compounds from advanced density-functional first-principles calculations, Phys. Rev. Lett. 108, 235502 (2012).
- [6] T. Björkman, Testing several recent van der Waals den-

- sity functionals for layered structures, J. Chem. Phys. **141**, 074708 (2014).
- [7] K. Berland, T. L. Einstein, and P. Hyldgaard, Rings sliding on a honeycomb network: Adsorption contours, interactions, and assembly of benzene on Cu (111), Phys. Rev. B 80, 155431 (2009).
- [8] W. Liu, V. G. Ruiz, G.-X. Zhang, B. Santra, X. Ren, M. Scheffler, and A. Tkatchenko, Structure and energetics of benzene adsorbed on transition-metal surfaces: Density-functional theory with van der Waals interactions including collective substrate response, New J. Phys. 15, 053046 (2013).
- [9] A. Bilic, J. R. Reimers, N. S. Hush, R. C. Hoft, and M. J. Ford, Adsorption of benzene on copper, silver, and gold surfaces, J. Chem. Theory Comput. 2, 1093 (2006).
- [10] F. Maaß, Y. Jiang, W. Liu, A. Tkatchenko, and P. Tegeder, Binding energies of benzene on coinage metal surfaces: Equal stability on different metals, J. Chem. Phys. 148, 214703 (2018).
- [11] H. Peng, Z.-H. Yang, J. P. Perdew, and J. Sun, Versatile van der Waals density functional based on a metageneralized gradient approximation, Phys. Rev. X 6, 041005 (2016).
- [12] J. Moellmann and S. Grimme, DFT-D3 study of some molecular crystals, J. Phys. Chem. C 118, 7615 (2014).